Mars seismology

Philippe Lognonné, W.B. Banerdt, J. Clinton, R.F. Garcia, D. Giardini, B. Knapmeyer-Endrun, M. Panning, W.T. Pike

Mars seismology

P. Lognonné[(1)], W.B. Banerdt[(2)], J. Clinton[(3)], R.F. Garcia[(4)], D. Giardini[(5)], B. Knapmeyer-Endrun[(6)], M. Panning[(2)], W.T Pike[(7)]

(1) Université Paris Cité, Institut de physique du globe de Paris, CNRS, F-75005, Paris, France.
(2) Jet Propulsion Laboratory, California Institute of Technology, Pasadena, CA, USA.
(3) Swiss Seismological Service, ETH Zürich, Zürich, Switzerland
(4) Institut Supérieur de l'Aéronautique et de l'Espace SUPAERO, Toulouse, France.
(5) Institute of Geophysics, ETH Zurich, Zurich, Switzerland
(6) Bensberg Observatory, University of Cologne, Bergisch Gladbach, Germany
(7) Department of Electrical and Electronic Engineering, Imperial College London, London, UK.

Abstract:

For the first time, from early 2019 to end of 2022, Mars shallow and deep interior have been explored by seismology with the InSight mission. Thanks to the performances of its seismometers and quality of their robotic installation on the ground, more than 1300 seismic events have been detected, including about 90 marsquakes at teleseismic distances, with Mw from 2.5 to 4.7 and 6 impacts, the largest ones with craters larger than 130m. A large fraction of these marsquakes occurs in Cerberus Fossae, demonstrating active regional tectonics. Records of pressure induced seismic noise and of heat flow penetration seismic signal have provided subsurface models below the lander. Deeper, direct and secondary body wave phases travel time, receiver function and surface waves analysis have provided the first interior models of Mars, including crustal thickness and crustal layering, mantle structure, thermal lithospheric thickness and core radius and state.

Keywords:

Mars, seismology, marsquake, impacts, Cerberus Fossae, interior structure

1. Introduction: past missions and InSight's birth

Mars seismology was long a dream before becoming a reality. It started with the Viking landers at the end of 1976 (Anderson et al. 1977). The Viking 1 seismometer failed to unlock, but the Viking 2 seismometer provided nearly 19 months of continuous records. However, its location on the lander's deck instead of ground meant it was overly sensitive to the wind (Nakamura and Anderson 1977, Lognonné & Mosser 1993) with no conclusive event detection. This pioneering mission nevertheless returned an important result, as summarized by D. L. Anderson: "One firm conclusion is that the natural background noise on Mars is low and that the wind is the prime noise source." This turned out to be a key specification for any future Mars seismology project.

Decades passed without any further seismic data from Mars. The Mars 96 mission, with 4 landers or penetrators with seismometers, failed post-launch in November 1996. Several other proposals failed to reach mission implementation (see Lognonné 2005, Lognonné & Johnson 2015 or Lognonné et al. 2019 for a list of these projects).

Finally, in 2012, NASA selected InSight (*Interior Exploration using Seismic Investigations, Geodesy and Heat Transport*, Banerdt et al. 2020) as the 12th Discovery mission, almost 30 years after the end of Viking 2 operation. With the seismic suite SEIS (*Seismic Experiment for Interior Structure of Mars*) as the primary instrument (Lognonné et al. 2019), the mission aimed to deploy the first Martian geophysical station equipped with a very-broad band (VBB) instrument comparable to those used by the Earth Global Seismic Network (Ringler et al. 2022). Additional payload elements were a high-precision tracking system for geodesy, a heat-flow experiment, a 3-axis magnetometer and more importantly for SEIS, a set of wind (TWINS, Temperature and Wind for INSight) and pressure sensors (Banfield et al. 2019, 2020) and a robotic arm and cameras, required to deploy SEIS on the ground. See Banerdt et al 2020 for further details.

Launched on May 5,2018, InSight landed successfully in Elysium Planitia (Golombek et al. 2020) on November 26, 2018 and deployed its seismometer shortly after. SEIS was still operating at the time of this writing in mid-2022 and this review presents the scientific results of almost 3.5 years of SEIS operation, since the start of its nominal operation in February2019.

After presenting the SEIS signal stream showing the recorded seismic and non-seismic noise, and introducing operation activities and data products, we will review the achievements of SEIS in terms of marsquake and impact detection, source characterization, and shallow subsurface, crust and deep-interior inversions and interpretation We will conclude with some lessons learned for future missions.

2. SEIS on Mars

SEIS has two 3-axis seismometers: Very Broad Band (VBB) and Short Period (SP). Both are mounted on a leveling system and include thermal and wind protection (Lognonné et al. 2019). Figure 1 illustrates the installation (details in Yana et al. 2022), which was critical for mission success as SEIS on the lander deck was twice as sensitive to wind as Viking (Panning et al. 2020).

The first seismic noise records (Lognonné et al. 2020) from the ground confirmed D. L. Anderson's predictions, with ultra-low night noise (down to $2x10^{-10}$ m/s^2/Hz$^{1/2}$ between 0.1-1Hz) but much larger amplitudes during the windy day, up to a few times 10^{-8} m/s^2/Hz$^{1/2}$. At night this is 1/500 of the low noise model (LNM, Peterson 1993) but during the day noise is above the Apollo minimum although still 1/10 of LNM (Figure 2). Despite the ground installation and shielding, comparison between SEIS noise and wind amplitude shows a significant sensitivity (Figures 3 A-B). The quietest periods mainly occur during early evenings in spring and summer when winds are below the resolution of TWINS. During windy periods and below 1 Hz, the noise is ground roll associated with the wind-carried pressure fluctuations, generating a larger noise on the vertical than horizontal (Figures 3 C-D). This was predicted (Lognonné & Mosser 1993, Murdoch et al. 2017) but is amplified by the very low rigidity of the near subsurface. Noise is therefore significantly polarized (Stutzmann et al. 2021). As predicted, pressure drops associated with atmospheric vortices (i.e., dust devils) contribute to this signal (Lorenz et al. 2015, Kenda et al. 2017). They have been extensively analyzed (Banerdt et al. 2020, Lognonné et al. 2020, Kenda et al. 2020, Lorenz et al. 2021, Murdoch et

al. 2021), along with complementary orbital characterization (Banerdt et al. 2020, Perrin et al. 2020), and have been used to invert for subsurface rigidity (see section 6.1). Part of this pressure loading noise can be corrected with pressure data (Garcia et al. 2020).

Lander vibrations are the major noise source above 1 Hz. Amplitudes are coherent with the quasi-static ground deformation from lander loading (Murdoch et al. 2017, Mimoun et al. 2017), but larger amplitudes are found around lander resonances suggesting SEIS rotation (Fayon et al. 2018) generated by tether motion. The amplitudes of these resonances depend strongly on wind and their frequency depends on ambient temperature (Dahmen et al. 2021). The Load Shunt Assembly (LSA), which partially decouples SEIS from cable motion (Hurst et al. 2021), generates weaker resonances in the SEIS signal. Lander resonance amplitudes nevertheless provide a remarkable indirect wind measurement (Dahmen et al. 2021). This allows development of co-modulation techniques (Charalambous et al. 2021) critical for wind-noise assessment of low amplitude seismic phases (e.g. Stähler et al. 2021), especially when wind sensors are not powered.

Whereas temperature variations for the martian atmosphere (and thus the unprotected tether) are larger than 80K, variations at the VBB sensor level are strongly reduced by the thermal protection to about 20K, (Lognonné et al. 2020, supplementary section 1). Insolation variations during eclipses can also be detected by SEIS (Stähler et al. 2020). Thermal variations generate deformation of the ground, thermal stresses in the tether and glitches, which are generally large compared to the seismic signal (Scholz et al. 2021, Ceylan et al. 2020). Glitch occurrence is not random, with daily repetition occurring at similar local time (e.g. Scholz et al. 2020 and Figure 3). Furthermore, glitches can occur in the form of sequences with stable time delays (Barkaoui et al. 2021). As shown by Kim et al. (2021), glitches impact auto-correlation analyses performed on raw data (e.g. Deng & Levander 2020) and therefore such analyses should only be made on deglitched data (e.g. Compaire et al. 2021) or on periods without glitches (e.g. Schimmel et al. 2021). Due to their impact on data time series, including during marsquakes (Figure 4), deglitching techniques have been proposed (Scholz et al. 2021) including machine-learning approaches (Barkaoui et al. 2021, Wuchuan et al. 2022).

SEIS is operated by CNES SISMOC (**S**e**IS** on **M**ars **O**peration **C**enter). The data curation and archiving are led by the IPGP **M**ars **S**EIS **D**ata **S**ervice (MSDS) for all SEIS data (Insight Mars SEIS Data Service 2019). VBB data are available with very little interruption from sol 73 to sol 1243, after which the VBBs operated partially each sol due to lander energy limitations. Daytime data from SP is available while SEIS was still on the lander deck, and SP was continuously monitored on the ground from sol 25 through sol 1061, when it stopped due to energy constraints. SP's self-noise prevents it from recording the background noise at the quietest times of the sol (Figure 3). Most of the analyses reviewed here are made with VBB channels.

The generation of the seismicity/event catalog is made by the **M**ars**Q**uake **S**ervice, (MQS, Clinton et al. 2018, Clinton et al 2021, Ceylan et al, 2022), led by ETHZ. MQS catalogs (InSight Marsquake Service 2020 for the first one) and MSDS SEIS data were released every 3 months. By the time of this review publication, all SEIS data through the end of 2022 (and therefore likely all mission data) is scheduled to be released, including the MQS catalog version 13 (InSight Marsquake Service 2023) covering the last trimester of 2022.

3. Marsquakes

Event detection was performed by MQS. Although tested before launch (Clinton et al. 2017, van Driel et al. 2018), the detection processes were significantly updated due to the intense scattering observed in marsquake records (Lognonné et al. 2020, Giardini et al. 2020). Although not as strong as on the Moon, seismic multi-path diffusion smooths impulsive arrivals and generates long codas (Lognonné et al. 2020, Menina et al. 2021, Karakostas et al. 2022), which reduces the number of events with clear P and S ballistic phases. In addition, waveform contamination by atmospheric disturbances, glitches and other non-seismic features of the SEIS data (Ceylan et al. 2021) challenged MQS operators. See Clinton et al. 2021, Ceylan et al. 2021, 2022 for more details on the techniques implemented.

When an event was confirmed, MQS provided, when possible, seismic phase arrival times assigned to crustal Pg and Sg; mantle-going P and S arrivals; or, rarely, their surface reflections (PP and SS, respectively). Secondary phases have also been reassessed for the purpose of interior model inversions (see section 6). Event quality is assigned to each event, ranging from A (best - located) to D (worst - very weak energy, possibly speculative), based on the phase picking and back-azimuth errors.

A rich set of seismic events have been observed by InSight; the majority have signal duration of 10s of minutes and a frequency-content classification has been made (Giardini et al. 2020, Clinton et al. 2021). During low background noise periods, the seismic data has a strong resonance at 2.4Hz (see Figure 2), excited by seismic events and weakly sensitive to wind (Dahmen et al. 2021). Hobiger et al. (2021) find it can be explained by a resonance in the geological structure beneath the seismometer.

The first family of events has energy predominantly below 2.4Hz, extending down to 10 seconds and sometimes even below. They are called low frequency (LF) if energy is only below 2.4Hz and broadband (BB) if energy also includes or exceeds this frequency. These events have similar characteristics and frequency content to teleseismic events observed on Earth, and P and S waves are often identified. The first significant LF event to be observed is shown in Figure 4 while the full collection of quality A and B LF/BB events is shown in Figure 5.

High frequency family events, shown in Figure 6, exhibit energy predominantly at and above 2.4Hz. Phases from these events are assigned as Pg and Sg and are interpreted as crustal guided waves (van Driel et al. 2021). Three types of events are observed. “2.4 Hz” events are those exciting only a narrow band around 2.4Hz. If energy is seen above 2.4Hz but not exceeding 10Hz they are labeled as High frequency (HF). Those with dominant horizontal components rising up to and beyond 10Hz are called very high frequency (VF). The last family is super high frequency (SF) events with a very short duration of ~10s, mostly on horizontal components and only above 5Hz. They occur predominantly around sunset on Mars, and are interpreted as local thermal cracking. A large number of these events have been identified using template matching (Dahmen et al. 2020).

Over 1300 LF/BB/SF MQS events have been identified as of 7/21/2022. 94 are LF family with 14 quality A and 20 quality B. 1223 are HF family, with 49, 76 and 25 of quality B for 2.4 Hz, HF and VF respectively. About 1300 SF events complete this list. Machine learning was recently used to explore the martian dataset and identify transient features (Barkaoui et al. 2021). Stott et al. (2022) detected additional seismic events using the wind and pressure channels. With a CNN approach and synthetic marsquake training dataset, Dahmen et al. (2022) generated a catalog replicating about 90% of the MQS events and extending the total

number by 60%. Additionally, Sun & Tkalcic (2022) used template matching of S-waves and found another 49 events.

When possible, event location is made with a probabilistic single-station procedure (Khan et al. 2016, Böse et al. 2017) that independently computes distance and back azimuth. Only three of the largest events include direct surface waves: two impacts (S1000a, S1094b, Kim et al. 2022, Posiolova et al. 2022) and one marsquake (S1222a, Kawamura et al. 2022). Only the latter has multi-orbit surface waves enabling its location (Panning et al. 2022) with the pre-launch R1-R2-R3 method (Panning et al. 2015, 2017). MQS located events only using direct body phase arrivals, e.g. the first arriving P and S-phase, without constraining depth. While pre-landing interior models (Clinton et al. 2017) were initially used for locating LF family events, since v11 MQS uses inverted models (Stähler et al. 2021, Ceylan et al. 2022). For HF family events, a simple single layer crustal model is used (van Driel et al. 2021). Amplitude-magnitude relations (Böse et al. 2018 and Böse et al. 2021 for post-launch recalibrated ones) provide the magnitude of those events assigned a distance. The back azimuth, when it can be ascertained, is obtained using polarization analysis of the first seconds of P and S body wave arrivals (Zenhäusern et al. 2022). Figure 7 shows the locations of about 25 LF events, with an area indicating locations for the HF cluster (Stähler et al. 2022). Figure 8 shows the distribution of marsquakes with respect to magnitude and epicentral distance. Only VF events are observed close to the lander, and have been observed out to 35°. HF and 2.4Hz events cluster between 20-30°. LF family events are also dominant at distances between 25-32° though some events are seen beyond the core shadow zone out to about 130° (Horleston et al. 2022). LF family events have the largest magnitudes, with S1222a reaching Mw4.7 and 3 others at or above M4.0. S1222a has very large amplitudes at high frequencies (Kawamura et al. 2022) and has likely generated avalanches near its epicenter (Lucas et al. 2022). Only one VF (S0976b) at 16° reaches Mw4, although another high amplitude VF signal was located at 50 km from InSight, with Mw3 (S1034a). Figure 7 also shows the magnitude detection threshold, as low as M1 for VF close to the lander and rising to M2 at 30°. For LF, it is about M2.5 and only M4 events and greater are seen beyond 100°.

Figure 9 shows how event amplitudes compare with the evolving background noise. The majority of events are only marginally above the lowest 10^{th} percentile of noise, and can be detected only during the quiet period. Only a handful of events are clearly above the noisiest periods and could be identified at any time of the mission. Knapmeyer et al. (2021) demonstrate that the changes in HF event rates during the first Martian year cannot be explained by background noise alone. There is a remarkable similarity between both background noise and event occurrence across the 2 Martian years monitored. Even if the largest events have all occurred during the second Martian year, the LF event rate in the second year is similar to the first year but the HF event rate is significantly higher (Ceylan et al. 2022, Dahmen et al. 2022).

4. Meteoroids airbursts and impacts

Detection of impacts was expected to be challenging given the estimated pre-launch rate of 1-10/year for impacts (Teanby et al. 2011, Lognonné & Johnson, 2015, Daubar et al. 2018) and 10-200/year for airbursts (Stevanović et al. 2017).

No clear seismic impact signal was identified during the first Martian year, including from a small, close (Daubar et al. 2020) and the arrivals of Mars landers (Fernando et al.

2021a,b). In contrast, 6 impacts have been detected and located during the second Martian year, which invites a re-analysis of the complete event catalog in the future.

Two different methods were used for locating impacts. For impactors closer than 300km, infrasound simulations predicted an acoustic waveguide close to the surface during the night (Garcia et al.2017, Martire et al. 2020). Dispersive acoustic signals from this waveguide were detected for 4 VF seismic events in the form of dispersive chirps with strong elliptical polarization pointing toward the impact source (Garcia et al. 2022). This allows location using differential times between among P, S and acoustic waves (Millour et al. 2018). CTX and HiRISE images confirmed fresh craters associated with these locations (Garcia et al. 2022).

At distances larger than 500 km, acoustic waves cannot be observed due to attenuation in the Martian atmosphere (e.g. Lognonné et al. 2016, Garcia et al. 2017). Consequently, the MQS location can be used for orbital imaging search. Two large fresh craters with diameter > 130m were associated to S1000a and S1094b (Posiolova et al. 2022) with high resolution imaging and a <3-sol time uncertainty, thanks to the global MARCI imaging system (Bell et al. 2009).

These impacts provide a relationship between crater diameter, impactor momentum and the seismic source parameters (seismic moment, source-time function). This is illustrated by Figure 10, with seismic moment estimated from the amplitudes of seismic waves (Garcia et al. 2022, Posiolova et al. 2022), and the impactor vertical momentum estimated from impact simulations constrained by size and distribution of ejecta (Collins et al. 2022). This confirms a power-law relation between seismic moment and impactor vertical momentum as predicted by models (Daubar et al. 2018 for review; Wójcicka et al. 2020). Source-time-function cutoff frequencies are 8-9 Hz, for crater diameters 4-6 m respectively, falling to 3 Hz at 130 m (Garcia et al. 2022, Posiolova et al. 2022), consistent with impact source models (Gudkova et al. 2015) once differences between the lunar and martian sub-surface have been taken into account. Apart from the source cutoff, no major waveform differences are found between impacts and marsquakes occurring at similar distances (Figure 5).

The known location is also critical for single-station inversions of differential seismic travel times, either in the crust (Garcia et al. 2022) or in the deep mantle (Posiolova et al. 2022), as well as surface wave analysis (Kim et al. 2022).

Finally, acoustic waves from airburst and impacts constrain the atmospheric temperature and wind structure (Garcia et al. 2022; Xu et al. 2022a), as well as the entry process in the atmosphere (Garcia et al. 2022).

5. Tectonics interpretation and source analysis

The clustered seismicity of Cerberus Fossae (CF, e.g. Perrin et al. 2022) (Figure 11a) is a major discovery of SEIS. Several 10s of LF and possibly more HF quakes originate from CF, including S0173a and S0235b with MQS Mw3.4-3.6 (Giardini et al. 2020, Clinton et al. 2021), later re-estimated by Centroid Moment Tensor inversion (CMT) to Mw2.9-3.2 (Brinkman et al. 2021, Jacob et al. 2022). Depth phases from these events provide depths ranging from 27-38 km (Duran et al. 2022) and 18-35 km (Drilleau et al.2022), similar to those found by CMT studies. As illustrated by Figure 11b, S0173a, S0409d, S0809a and S0820a have mechanisms close to the general direction of CF grabens (Jacob et al. 2022), and the strike direction of S0235 normal fault is also along this direction (Brinkman et al. 2021, Jacob et al. 2022). Jacob et al. (2022) also demonstrated that these mechanisms did not excite surface waves above

the VBB long period noise. This is indirectly confirmed by S1222a with its modest SNR for R1 surface waves (Kawamura et al. 2022).

Source cutoff and attenuation have inherent trade-offs for single station analysis. With $Q\mu > 800$ at 0.5 Hz from coda analysis of S0235b (Lognonné et al. 2020), lithospheric shear $Q\mu$ is on the higher side compared to the pre-launch analysis (Smrekar et al. 2019). Giardini et al. (2020) suggested larger apparent Q_s deeper in the mantle. Due to the low $Q\mu$ at Phobos tidal period (e.g. Lognonné & Mosser, 1993), this suggests a frequency dependence of attenuation greater than for the Earth (Bagheri et al. 2019, Harada, 2022). Assuming intrinsic attenuation to be dominant along P and S paths, Stähler et al. 2022 proposes slow rupture processes for the ~15 LF/BB events located near CF as the consequences of warmer conditions at seismogenic depth. They suggest a CF present seismic activity of 1-5 10^{15}N/yr, about 1-2% of the 10My average (Taylor et al. 2013). Although the moments of the largest CF events are an order of magnitude too large to be tremors (Kedar et al. 2021), the CF activity could be compatible with dyke-induced seismicity (Rivas-Dorado et al. 2022, Stähler et al. 2022), from small but still active intrusions (Sun and Tkalčić, 2022). On a global scale, Mars seismicity (Banerdt et al. 2020) is significantly lower than pre-launch estimation (Plesa et al. 2018, Knapmeyer et al. 2019) and was re-estimated to 6.5-17 10^{15}N/yr (Knapmeyer et al. 2022). See da Silva and Corso (2021) for further comparison with Earth.

6. Interior structure analysis

6.1 Subsurface

V_p and v_s in the uppermost decimeters below SEIS were obtained by using the hammering of the HP^3 heat flow probe (Spohn et al. 2019) as a repeatable, active source (Lognonné et al. 2020, Brinkman et al. 2022). This required synchronization of clocks between HP^3 and SEIS and special data processing (Sollberger et al. 2021, Brinkman et al. 2019, Kedar et al. 2017). Analysis provided v_p and v_s in the range of 98-163 m/s and 56-74 m/s respectively in the first 30 cm (Brinkman et al. 2022), close to pre-mission estimates (Morgan et al. 2018) and in line with the surface rigidity constrained ground resonances (Lognonné et al. 2020).

Other subsurface constraints come from passing dust devils, which can be measured both in pressure recordings in the form of abrupt pressure drops and by SEIS in the form of ground tilt. This constrains the ground rigidity, i.e. the compliance, and through inversion provides a depth profile of Young's modulus and, by extension, seismic velocities (Lorenz et al. 2015, Kenda et al. 2017). Initial results with 150 sols of data provided constraints to about 20 m depth, with a clear increase in Young's modulus with depth, compatible with a regolith thickness between 0.7 and 7 m, and a significantly stiffer layer below (Lognonné et al. 2020, Kenda et al. 2020). A complementary analysis hinted at possible variations in elastic ground properties around SEIS, with harder, less deformable ground to the west, where rocky terrain is located (Murdoch et al. 2021). The full data set and refined analysis will allow an increase in vertical resolution and constrain deeper structure (Onodera, 2022).

Additionally, SEIS's VBBs horizontal-to-vertical spectral ratios (H/V) were used to constrain the shallow subsurface structure (e.g. Knapmeyer-Endrun et al. 2018). An initial

analysis considered frequencies between 1.5 and 8 Hz (Hobiger et al. 2021), including a pronounced H/V trough at 2.4 Hz related to a spectral peak on the vertical component. Assuming Rayleigh waves as the main component of the ambient background wavefield, the H/V inversion revealed several layers with altering high and low velocities. Subsequent analysis focused on the S-wave coda of marsquakes (Carrasco et al. 2022), since the ambient wavefield could be biased by amplitudes close to the instrument self-noise for periods of low wind and the influence of lander modes for higher winds (Mahvelati & Coe, 2021, Xio & Wang 2022). In the 0.4-10 Hz bandwidth, an additional H/V peak around 8 Hz was found and inverted with a diffusive wave field approach, i.e. considering body and surface wave contributions. Due to the depth-velocity trade-off inherent in H/V inversions, models are non-unique, but all share some common features, regardless of whether the 2.4 Hz trough is included in the inversion or not. The data require a shallow high-velocity layer beneath the surficial regolith, with v_s increasing somewhere in the top 15 m from less than 500 m/s to more than 1000 m/s. Below this high-velocity layer, interpreted as Amazonian lava flows, lower velocities compatible with a sedimentary layer could extend to 85 m deep. Below this, velocities increase again, but remain lower than in the Amazonian lavas, which could indicate a more physically or chemically weathered basaltic unit. These layered models down to 100 m depth are compatible with the lower-resolution compliance data (Carrasco et al. 2022).

While the early Suemoto et al. (2020) analysis on subsurface seismic velocity variation with temperature is likely corrupted by the temperature sensitivity of the 6.8Hz lander resonance (Kim et al. 2021), recent analyses (Compaire et al. 2021) used long term climatic variations, which diffuse deeper in the ground, and find at 8Hz seismic variation of 0.25%/°C.

6.3 Crust

The first constraints on crustal layering were derived from receiver functions (RF), using P-to-S converted phases from two CF marsquakes (Lognonné et al. 2020). They identified a first interface at 8-11 km depth beneath InSight, with low SV-wave velocities of 1.7-2.1 km/s above. Such low velocities require more than 20% unfilled porosity in basalt (Heap 2019) and exclude the presence of an aquifer (Manga & Wright 2021). This depth was confirmed by Li et al. (2022a), who found even lower SH-velocities. The velocity difference can be explained by 10-30% radial anisotropy caused by approximately East-West oriented intrusions, e.g. gas-filled fractures or igneous dikes. The thickness was again confirmed by SsPp phase detections (Li et al. 2022b), with v_p proposed in the range of 2.5-3.3 km/s and a porosity of 21 to 31%.

The deeper crustal structure beneath InSight was investigated with RFs and autocorrelations (Knapmeyer-Endrun et al. 2021). This confirmed the first layer, but additionally required either a single second discontinuity, 20±5 km deep, or two discontinuities, the first again located at 20±5 km depth, and a second weaker one at 39 ± 8 km depth. In both cases, the deeper discontinuity is interpreted as the crust-mantle interface (Figure 13a). Due to the overlap between direct conversions and multiple converted and reflected phases in the P-to-S RFs, and the inability to clearly identify multiple arrivals in the noisier later part of the

data, this analysis could not distinguish between the two possible model classes. Vertical component autocorrelations (Deng & Levander 2020, Compaire et al. 2021; Schimmel et al. 2021) contain clear P-wave reflections from the first two discontinuities, but cannot exclude the existence of a deeper, third discontinuity. The layered structure is also in agreement with a refraction seismic interpretation of P-wave arrivals from impacts within 300 km of InSight (Garcia et al. 2022); however, due to the small number of data points, this analysis is not unique. Later RF studies including additional events (Duran et al. 2022), phases (Kim et al. 2021), or more sophisticated data analysis (Joshi et al. 2022) favor the three-layer crust on the order of 40 km thickness beneath InSight. This seismic anchor point has been used for a global crustal thickness map (Wieczorek et al. 2022) based on orbital gravity and topography measurements (Figure 13) and suggests a global mean crustal thickness in the range of 30-72 km for the three-layer model.

The crustal structure away from the landing site has been constrained with the PP and SS precursors S0976a, about 146° epicentral distance (Li et al. 2022c), with a bounce point halfway along the raypath (Figure 13e-f). They show a clear signal from a discontinuity about 20 km deep, with S-wave velocities around 2.2 km/s above, as in the second crustal layer beneath the lander, but no indication of any shallower strong impedance contrast (Figure e). An impedance contrast comparable to the one below InSight at 40 km depth cannot be resolved. This suggests that the shallowest discontinuity at about 10 km beneath InSight is not a global feature, a point corroborated by surface wave analysis of the largest impacts (Kim et al. 2022) and marsquakes (Li et al. 2022d, Xu et al. 2022).

Velocity models derived from the Rayleigh wave group velocities of two impacts north of the hemispheric dichotomy, averaging over the crust along the ray paths, find rather constant v_s around 3.2 km/s for depths between 5 and 30 km (Figure 13b-c), but no shallow, low-velocity layer as beneath the landing site (Kim et al. 2022). They also imply a higher crustal density away from the lander, which could be related to differences in composition or a reduction in porosity. S1222a provides additional dispersion measurements along both minor and major arc (Figure 13d), covering ray paths also traversing highland crust (Beghein et al. 2022, Li et al. 2022d, Xu et al. 2022b). While results for the lowlands are comparable to those derived from impacts, larger velocities beneath the highlands are required.

6.4 Mantle and core

Several studies have constrained the seismic velocities of the martian mantle and the core radius. These studies have relied upon matching secondary travel times of seismic phases in addition to the direct P and S phases (Figure 11). This includes phases reflecting from the surface (PP, PPP, SS, SSS) and from the core-mantle boundary (ScS) (Khan et al. 2021; Stähler et al. 2021; Duran et al. 2022; Drilleau et al. 2022; Khan et al. 2022). This is complementary to models fitting the free core nutation (Le Maistre et al. 2022) as determined by RISE (Folkner et al. 2018).

The studies above use different aspects of the seismic data, based on models with differing constraints (Mars measured moment of inertia, k_2 tidal Love numbers, and free core nutation estimates). All studies included event relocation during the velocity inversion

process. While the overall dataset of travel times across these studies converges (albeit with more events included in later studies and some differences in precise travel-time picks), the remaining differences seen in the velocity models relate to the choices made in the inversion process. While most use a similar Bayesian inversion (e.g. Panning et al. 2017), several different approaches for parameterizing the forward models are used. These can be divided into three classes: 1) seismic models which directly parameterize the seismic velocity and density, 2) geophysical models which parameterize the chemical composition of the mantle and core and a range of assumed temperature profiles and then calculate the resulting seismic profiles using mineral assemblages calculated from Gibbs free energy minimization (e.g. Khan et al. 2021), and 3) geodynamic models which perform an additional step to determine possible thermal profiles from modeling thermal evolution of Mars using a range of rheological properties for the planet (e.g. Drilleau et al. 2021). Stähler et al. (2021) describe these classes of models in more detail. Despite this range in approaches, the general patterns resolved for seismic structure within the mantle (Figure 13) are very similar across the models. In particular, the shear velocity shows negative gradients as a function of depth down to ~400-600 km. This is consistent with a steeper temperature gradient (estimated at 2-2.9 K/km, depending on the study) within a thermal lithosphere down to this depth, with a more adiabatic temperature gradient in the convecting mantle below. The thermal profile at this greater depth is often defined by a mantle potential temperature, but estimates of this vary from relatively cool values of 1600-1750 K (Khan et al. 2021, Duran et al. 2022) to a warmer 1800-1900 K (Drilleau et al. 2022). Most models also show a significant jump in seismic velocity near ~1000 km depth, although this feature is primarily driven by a predicted mineral phase transition in the geophysical and geodynamic models, and is not yet directly constrained by the seismic observations as demonstrated by the lack of a sharp transition in the seismic models of Drilleau et al. (2022). The recent detection of Pdiff (Horleston et al. 2022) from the S1000a impact (Posiolova et al. 2022) will add new constraints on v_p near the core-mantle boundary.

To date, the core radius has only been constrained seismically by core-reflected S phases (ScS; Stähler et al. 2021), which are visible in several events after polarization filtering that emphasizes the near-vertically propagating S waves reflecting from the core. Such data can be combined with nutation measured via the RISE experiment (Le Maistre et al. 2022), which also gives information about core-density structure. The amplitude of the observed ScS phases supports a liquid core, and after inverting for both core radius and mantle velocity structure, a core radius of 1830 +/- 40 km is estimated. This is at the large end of pre-mission expectations (e.g. Smrekar et al. 2019), and implies a relatively low-density core (5.7-6.3 g/cm^3) in order to match constraints such as mass and moment of inertia. Mantle models with basal layers (Samuel et al. 2021) might provide alternatives for a smaller core (Le Maistre et al. 2022) but remain to be confirmed.

6 Lesson learned for future missions

InSight confirmed Mars to be a seismically active planet with elevated seismicity at Cerberus Fossae in addition to a weaker global activity. But half of the planet remains unexplored, as quakes < M3.5 cannot be detected in the core shadow zone.

Completing global coverage will therefore be a key objective for future projects. However, Anderson's admonition remains ironically valid. Major improvements in terms of

noise could be reached if VBB-like seismometers are deployed on bedrock, in order to reduce wind-induced surface deformations. This will lower the daytime detection threshold and better record the seismic noise of the planet, including its hum (Nishikawa et al. 2019). Most likely this will require mobility and a rover able to carry the geophysical package to such a bedrock, in addition to a thin cable able to decouple sensors from thermo-elastic stresses affecting the cable. This is the most promising direction for improving post-InSight deep interior models of Mars with new seismic data.

A complementary project would be to target Cerberus Fossae (Stähler et al. 2022b) and its regional crustal structure and seismicity. Seismic signals, especially those above 1 Hz, will have larger amplitudes closer to the epicenter, perhaps enabling a less sensitive seismometer compatible with regional networks implemented with semi-hard landing techniques and smaller landers.

7 Conclusion

InSight and SEIS are close to the end of their mission due to dust accumulation on solar panels. The comprehensive data set from SEIS provides major constraints on not only Mars seismicity and internal structure down to the core, but also seismo-acoustic coupling, both from impacts and atmospheric activity.

Future work will improve interior models, search for hidden seismic or infrasound events (Garcia et al. 2021, Ortiz et al. 2022), particularly with machine learning (Dahmen et al., 2022, Stott et al., 2022) and search for phases or long period signals not yet confirmed, including PKP phases (Irving et al. 2022), surface wave overtones (Xu et al. 2020), normal modes (Lognonné et al. 2022) and tides (Pou et al. 2021). As has been seen for the Apollo Lunar Surface Experiment (Bates et al. 1979), we can expect decades of scientific analysis with SEIS and InSight data.

Acknowledgments

We acknowledge NASA, CNES, their partner agencies and Institutions (UKSA, SSO, DLR, JPL, IPGP-CNRS, ETHZ, IC, MPS-MPG) and the flight operations team at JPL, SISMOC, MSDS, IRIS-DMC, PDS and MQS for providing SEED SEIS data and MQS catalogs. We thank the following SEIS team members, who provided figures to this review: M.Plasman (Figure 2), S.Ceylan (Figure 6,8), A. Jacob, G.Zenhäusern (Figure 7), A. Horleston (Figure 8), S.Stähler (Figure 9), M.Drilleau (Figure 11). PL and RG acknowledge the French Space Agency CNES and ANR (ANR-19-CE31-0008-08; ANR-18-IDEX-0001). This is InSight contribution number 300.

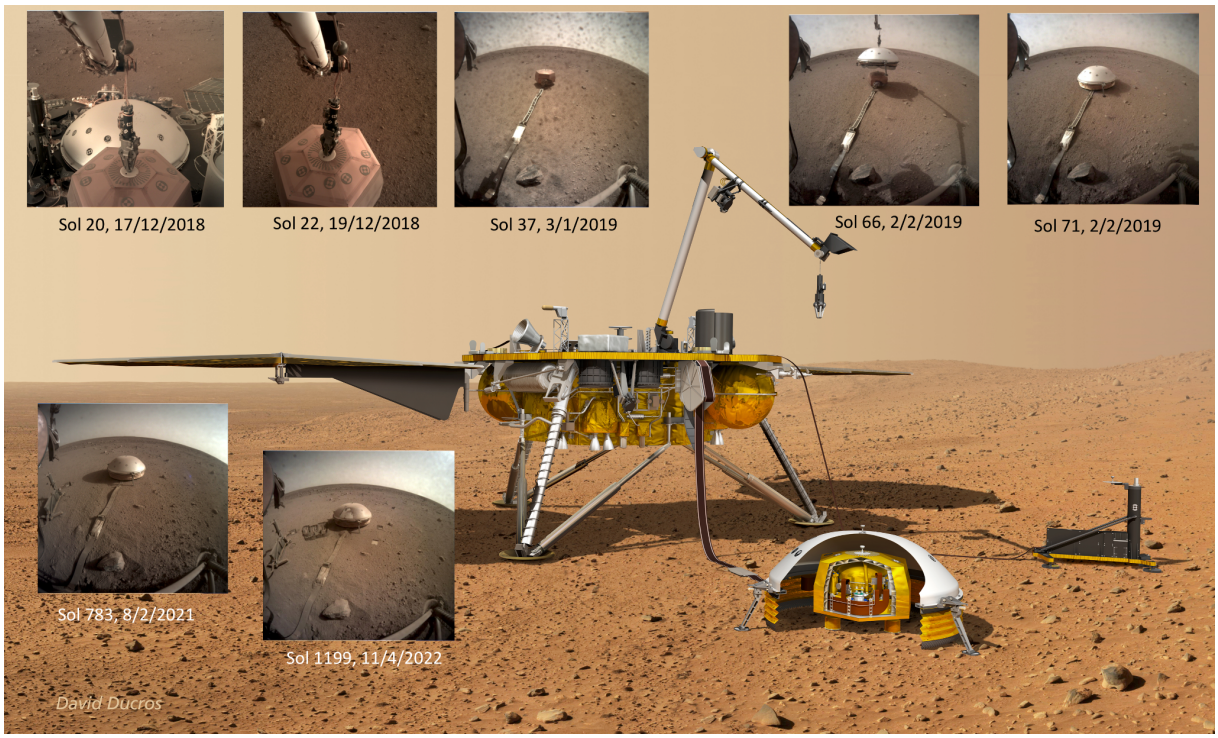

Figure 1: SEIS on Mars. This composite figure shows pictures taken by InSight cameras (Maki et al. 2018) during the different phases of SEIS installation on Mars performed by InSight's robotic arm (Trebi-Ollennu et al. 2018), from its post-landing extraction from the lander deck (sol 20), its surface installation (sols 22 and 37), tether deployment and azimuth determination (Savoie et al. 2021), Windshield deployment (sol 66) and start of operation in final configuration (sol 71). Two additional pictures show SEIS long after HP3 deployment, and SEIS after the tether burial effort. The artistic view provides a general view of SEIS with respect to the lander and HP3, as well as a cut-away illustrating the 3 layers of thermal protection, e.g. VBB vacuum chamber, Thermal Blanket and wind shield. See Lognonné et al. 2019 for further details.

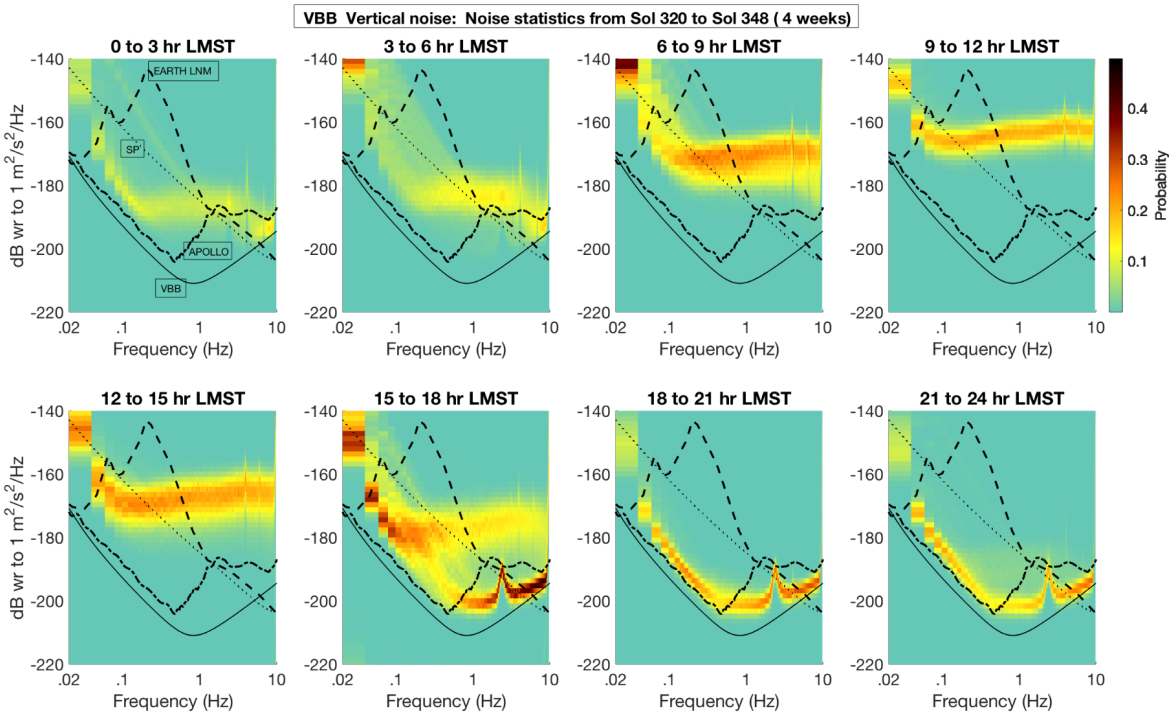

Figure 2: VBBZ ground velocity spectral density noise statistics for 4 weeks during sols 320 and 348 (sol is martian day; landing = sol 0). This corresponds to a period during which the early night low noise seismic window is the quietest (See Figure 3). Noise probabilities are shown in color. The VBBZ instrument self noise is shown by the solid line, while the SPZ self noise is shown by the dotted line. Apollo noise, made as composite from both the peaked LP and the SP (Lognonné & Johnson, 2015) is the dashed dot line. Earth Low Noise Model is the long dash line. During the late evening until almost midnight, a very stable low noise is achieved, revealing a resonance at 2.4 Hz. See main text for further discussion of the 2.4 Hz resonance. Outside this low noise period, broadband noise is observed, relatively flat in ground velocity, with an amplitude increasing during the day and reaching maximum around noon. Bimodal noise distributions are observed during 15-18 hr LMST and 21-24 hr LMST, corresponding to alternating low/high wind. Spectral amplitude estimates are made with 200 sec windows and the data have been corrected for the 1 Hz tick noise, a data acquisition artifact (Zweifel et al. 2021). Note above 1 Hz several sharp resonances associated with the lander (Dahmen et al. 2021) or tether system (Hurst et al. 2021).

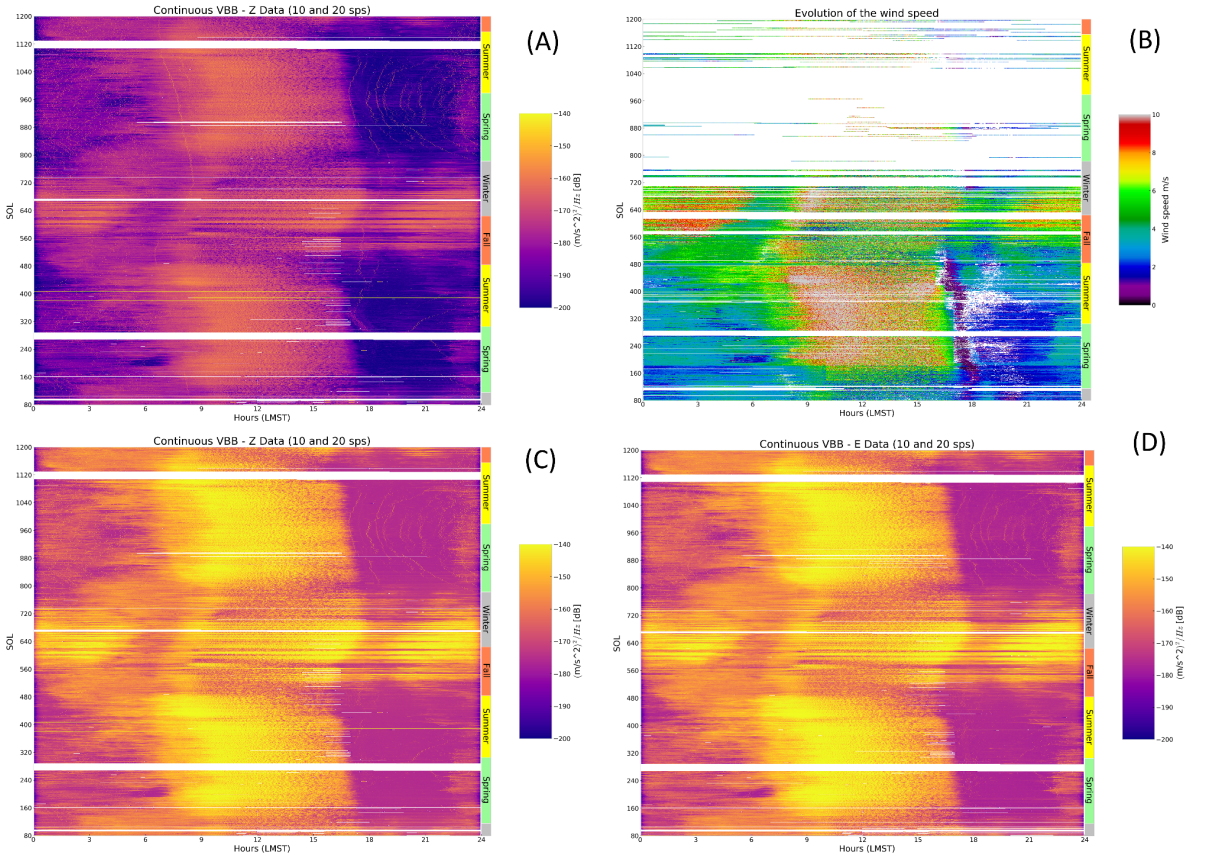

Figure 3: Seasonal variation of the VBB recorded ground acceleration noise, for the Z component (A and C) and for the East component (D). (A) is for the bandwidth 0.1-0.95 Hz, while C and D are for the bandwidth 1.5-8 Hz. All amplitudes are in db with respect to 1 m2/s4/Hz acceleration spectral power, from -200db (10^{-10} $m/s^2/Hz^{1/2}$) to -140db (10^{-7} $m/s^2/Hz^{1/2}$). Figure B provides the amplitude of the wind, as recorded by TWINS. All images cover the period from Sol 80 to 1200. The gaps in wind data (in white) are related to power limitation during the extended mission or to wind speeds below the sensor resolution. On the VBBs, small structured dots are associated with glitches occurring mostly during the cooling phase. See main text for more discussion.

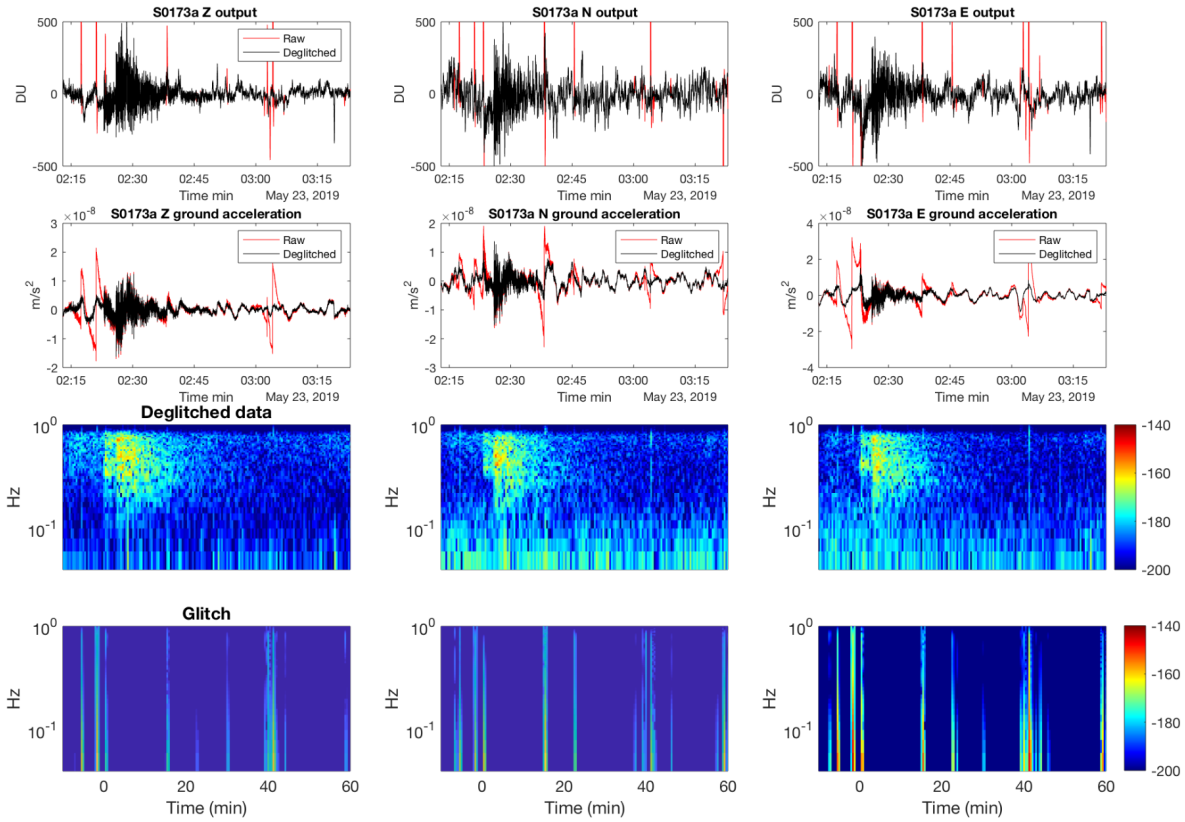

Figure 4: First low frequency event (S0173a), detected on May, 23, 2019. Data shown are those from the VBB output, when sampled at 2sps. The data have been deglitched using the IPGP deglitching techniques (Lognonné et al. 2020, Scholtz et al. 2021). Raw data are in red, while deglitched data are in black. The first line provides the outputs in Digital Units (DU) of the VEL VBB High Gain, after equalization of the V and W transfer functions with U and rotation into Z, N, E. The second line provides the ground acceleration for Z, N, E directions. The amplitude of this quake in terms of ground acceleration is < 10^{-8} m/s^2 in the 0.1-1 Hz bandwidth, illustrating the need for a low noise-high resolution sensor such as the SEIS VBB. Spectrograms for each component are shown, after deglitching on the third line, while the 4th line shows the glitches only. Unit for spectrograms are acceleration spectral density, in db with respect to 1 m^2/s^4/Hz.

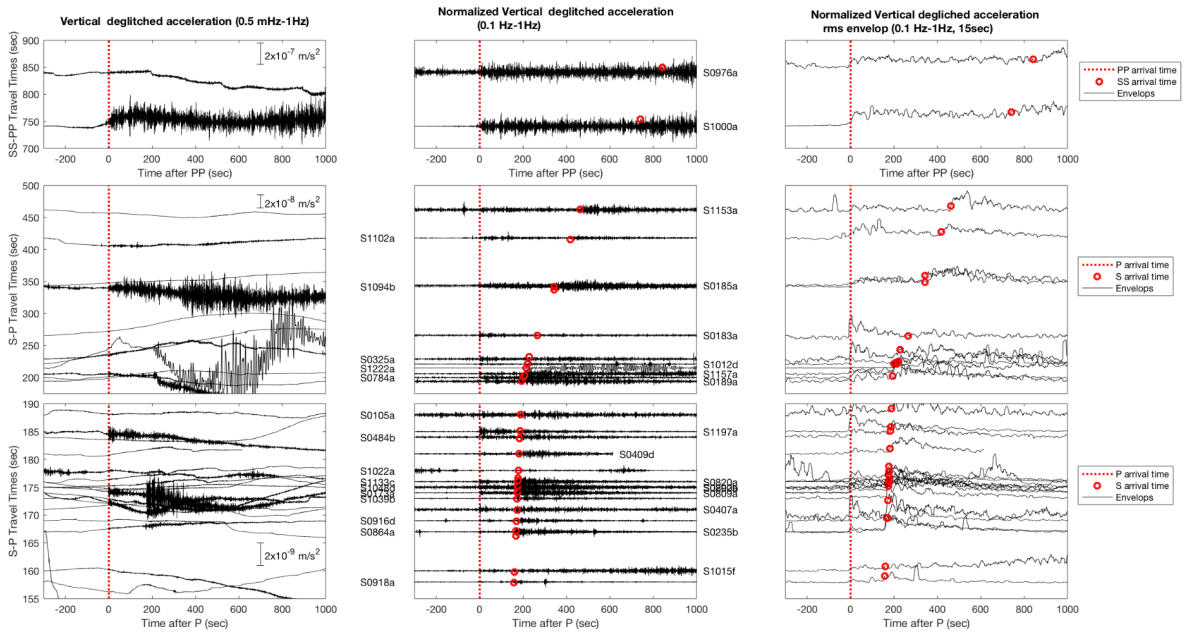

Figure 5: Collection of all 34 Quality A and B LF and BB events detected until S01222a. The three columns provide the vertical deglitched VBB acceleration in the 0.5mHz-1Hz bandwidth, the 0.1 Hz-1Hz bandpass signal and its rms envelope, with a moving window of 15 sec. All data are aligned with respect to the P arrival, or PP for the two events occurring in the shadow zone of the core (S1000a and S0976a). The S (bottom panel) or SS (top panel) arrival times are provided with red circles. Alignment is made with the P or PP measured travel time. Note that for S-P differential travel times around 175s the clusters are possibly associated with aftershocks or close active faults of events occurring in the Cerberus Fosse area. Note also that the envelope of S0185a marsquake is very similar to S1000a impact below 1Hz, when amplitude scaled.

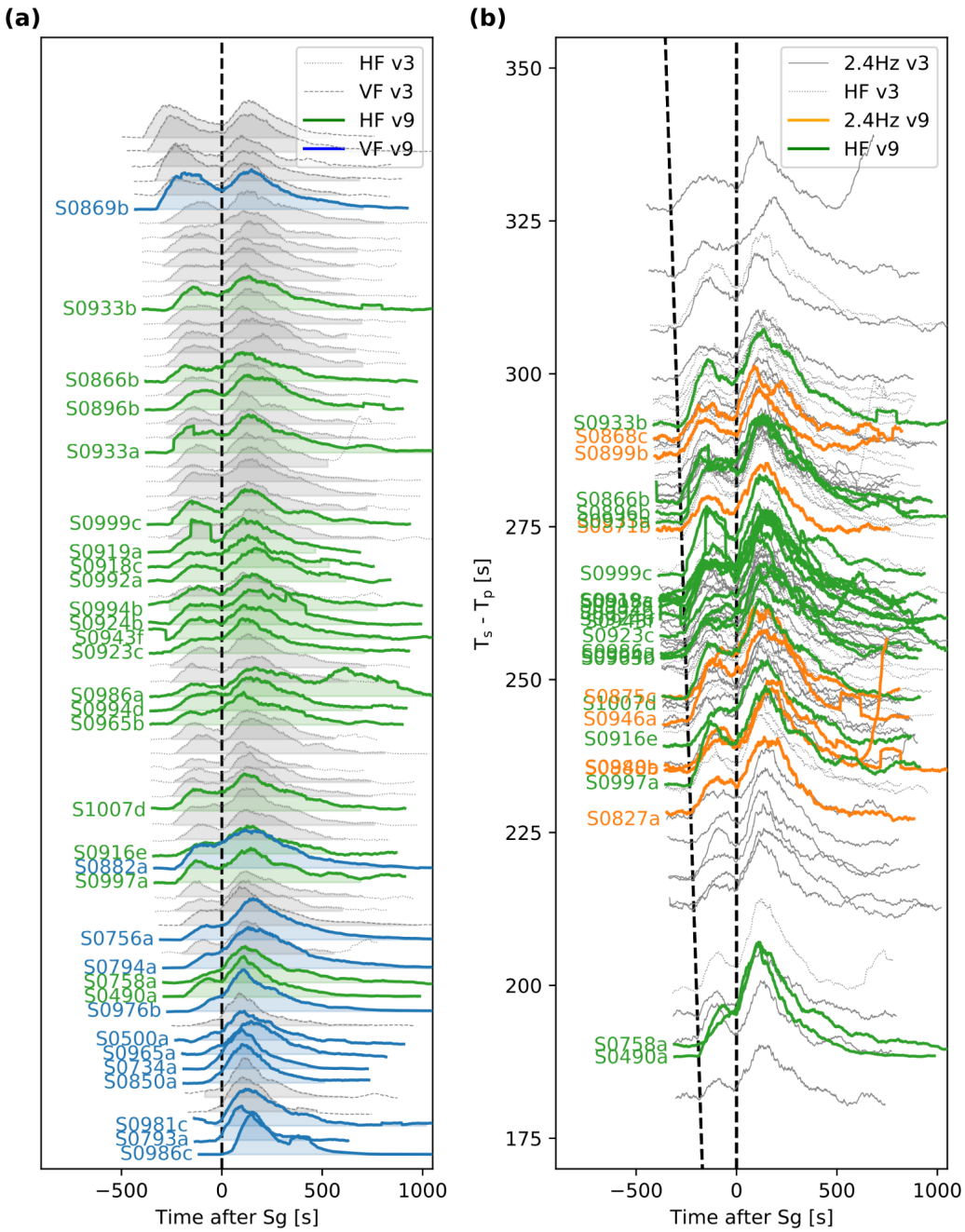

Figure 6: Envelopes for quality B high-frequency family events. (a) HF and VF aligned on the Sg arrivals, sorted by distance with regular spacing, and (b) HF and 2.4Hz events ordered by Ts--Tp differential times. The events reported in the V3 catalog are plotted in gray, while colored envelopes show V9 events. The envelopes are normalized and computed using the vertical component of VBB. The figure follows van Driel et al. 2019.

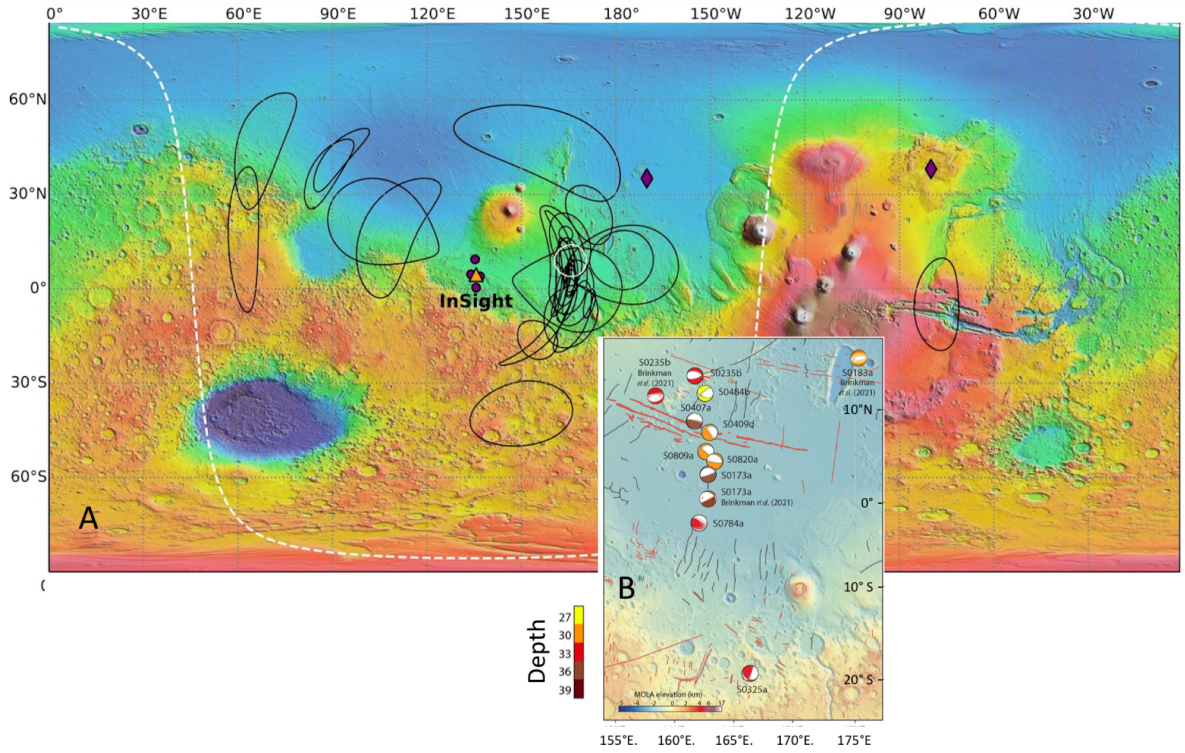

Figure 7: (A) Map of seismicity on Mars. Orange triangle indicated position of InSight lander. Black ellipses indicate LF family event location uncertainty ellipses from V12 MQS catalog (preferred), with additional events from Zenhäusern et al. (2022) and Drilleau et al. (2022). Purple colors indicate location of events detected by SEIS and confirmed as impact by satellite imaging - diamonds indicate large impacts at teleseismic distances, and circles smaller impacts within a few 100km of the lander. The white circle indicates the location of the HF events cluster described in Stähler et al. (2022a). The dotted white line is at 90° distance from InSight. Background color map uses Mars Orbiter Laser Altimeter elevation data (Smith et al. 2001). (B) Details of the CMT mechanisms proposed by Jacob et al. 2022 and, when specified, Brinkman et al. 2021. Locations are those of MQS for the three events analyzed by Brinkman et al. (2021) and those of Drilleau et al. (2022) for those of Jacob et al. (2022). The map also provides the main faults near the CF system.

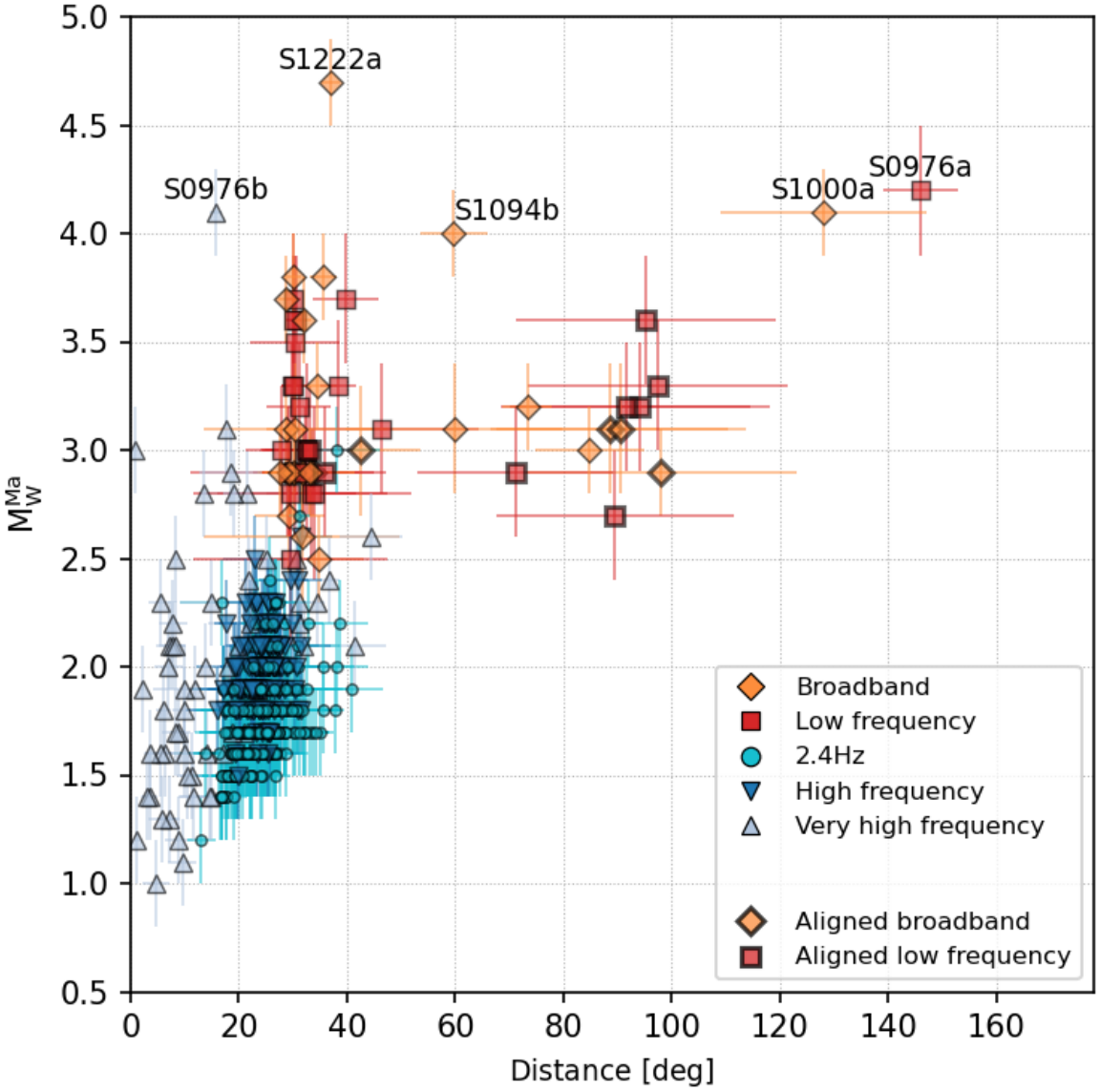

Figure 8: Distance and Mars-calibrated moment magnitude (Mw^{Ma}) distribution of the events included in the V12 catalog. The magnitudes are computed following Böse et al. (2021). The events with M≥ 3.9 are labeled. Two of them are impacts (S100a and S1094b) for which these magnitudes should not be seen as those of marsquake sources (Posiolova et al. 2022). Markers with thicker edges indicate the events that have a distance from alignments. Other events have been located using the MQS phase picks.

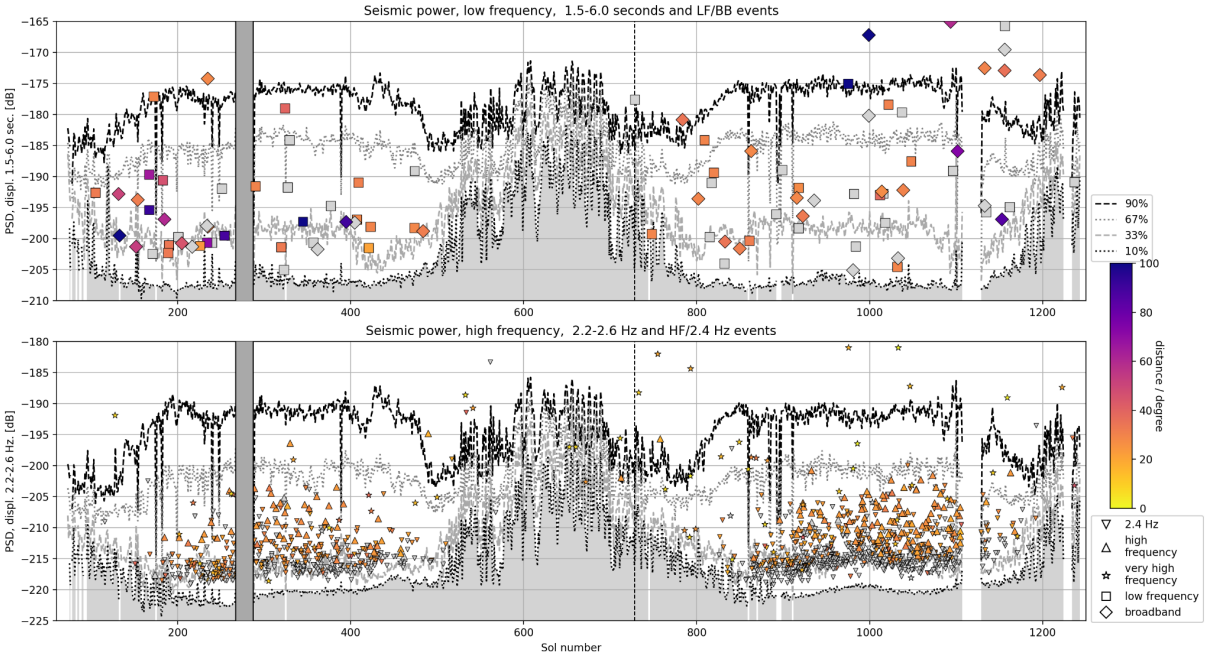

Figure 9: Summary image showing the evolving Martian background noise as recorded by the VBB vertical component as well as the occurrence, amplitude and distances of LF family (top) and HF family (bottom) marsquakes in the V12 catalog. Symbols indicate the marsquake event type and color bar shows event distances. Percentiles of the noise for each sol are indicated. Note the clear evolution of noise amplitudes across the seasons and the repeating noise levels from year to year. The first full Martian year ends on sol 740, indicated by the vertical dashed line. The extended periods of low noise in spring and summer coincide with the routine detection of HF events. The noise evolution at longer periods and at 2.4 Hz follow the same trends. The largest event, S1222, at -140dB, is not shown.

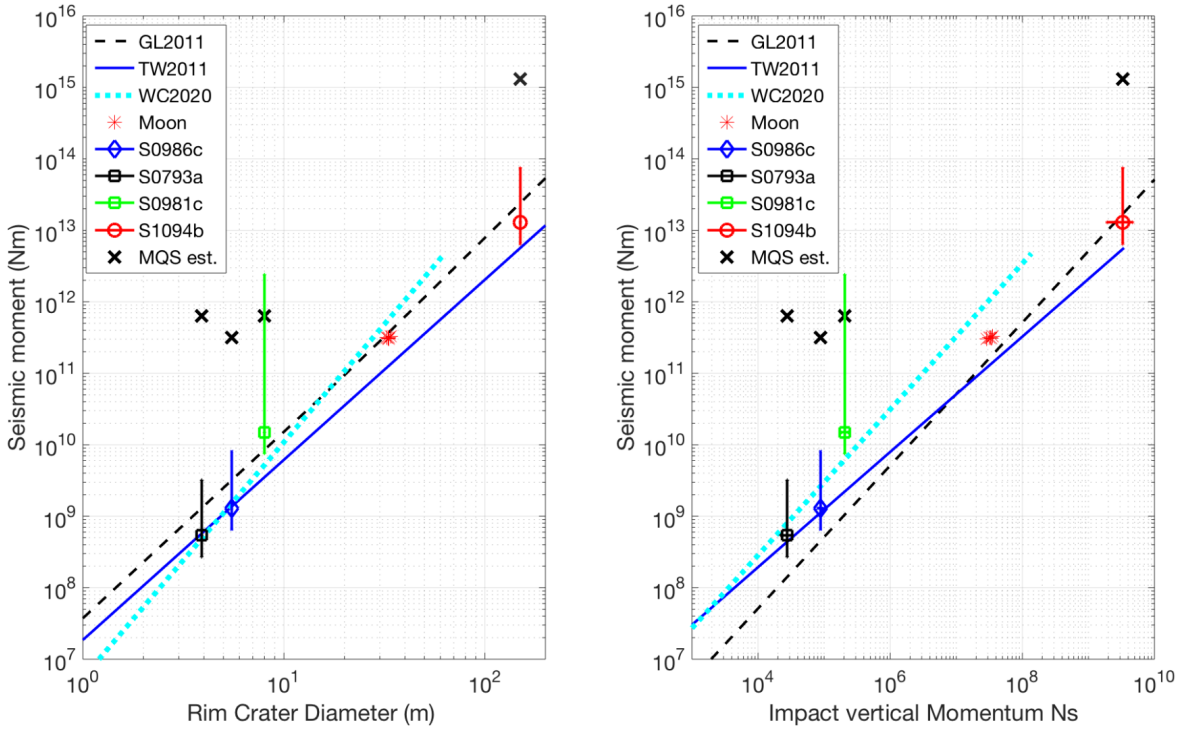

Figure 10: Seismic moment as a function of crater diameter (on the left) and impactor vertical momentum (on the right) estimated for 4 located impacts with moment and impulse estimations (Garcia et al. 2022; Posiolova et al. 2022), for Lunar artificial impacts (Lognonné et al. 2009), and for various impact/seismic models (Gudkova et al. 2015, Teanby & Wookey 2011, Wójcicka et al. 2020). See Daubar et al. (2018) for details on models.

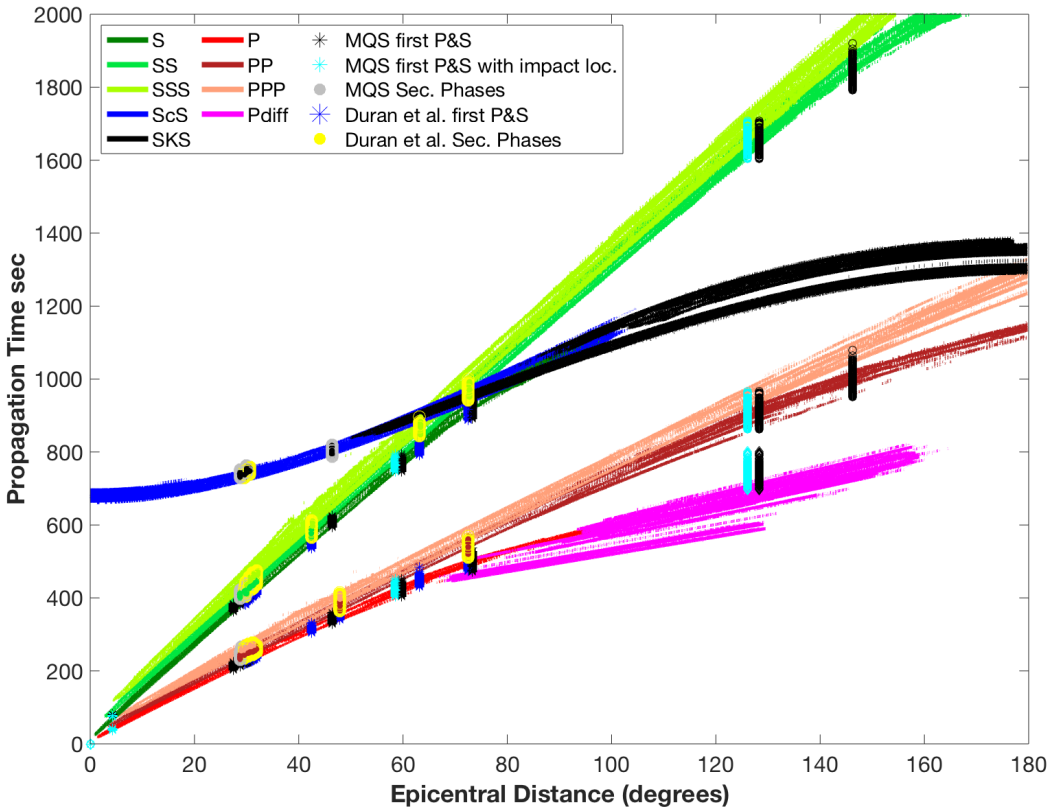

Figure 11: Comparison between hodochrones computed from published models and the different arrival times provided by MQS and the associated publications. The hodochrones provide the first arrival times, as function of epicentral distance of P, PP, PPP (red-tone colors), S, SS, SSS (green tone color), ScS (blue), SKS (black), Pdiff (magenta). See Legend for colors. These hodochrones show, in contour lines, the 10%, 35%, 75% of the a-posteriori probability of arrival times from the different sets of models from Stähler et al. 2021, Duran et al. 2022, Drilleau et al. 2022. Observed travel times from MQS (InSight Marsquake service, 2022, v11) are shown with black stars for the P and S arrival times and in colored dots with gray circles for secondary arrivals, with the same color code as the hodochones. Observed travel times from Duran et al. 2022 are shown with blue stars for P and S, and same convention as above for the secondary phases, but with a yellow circle. Cyan stars are used for impacts (4.25° for S981c, 58.5° for S1094b and 126.09° for S1000a) together with associated MQS arrival times. The Pdiff MQS arrival time of S1094b (Horleston et al. 2022) is also indicated with black/cyan stars overlaying the magenta Pdiff hodochrones.

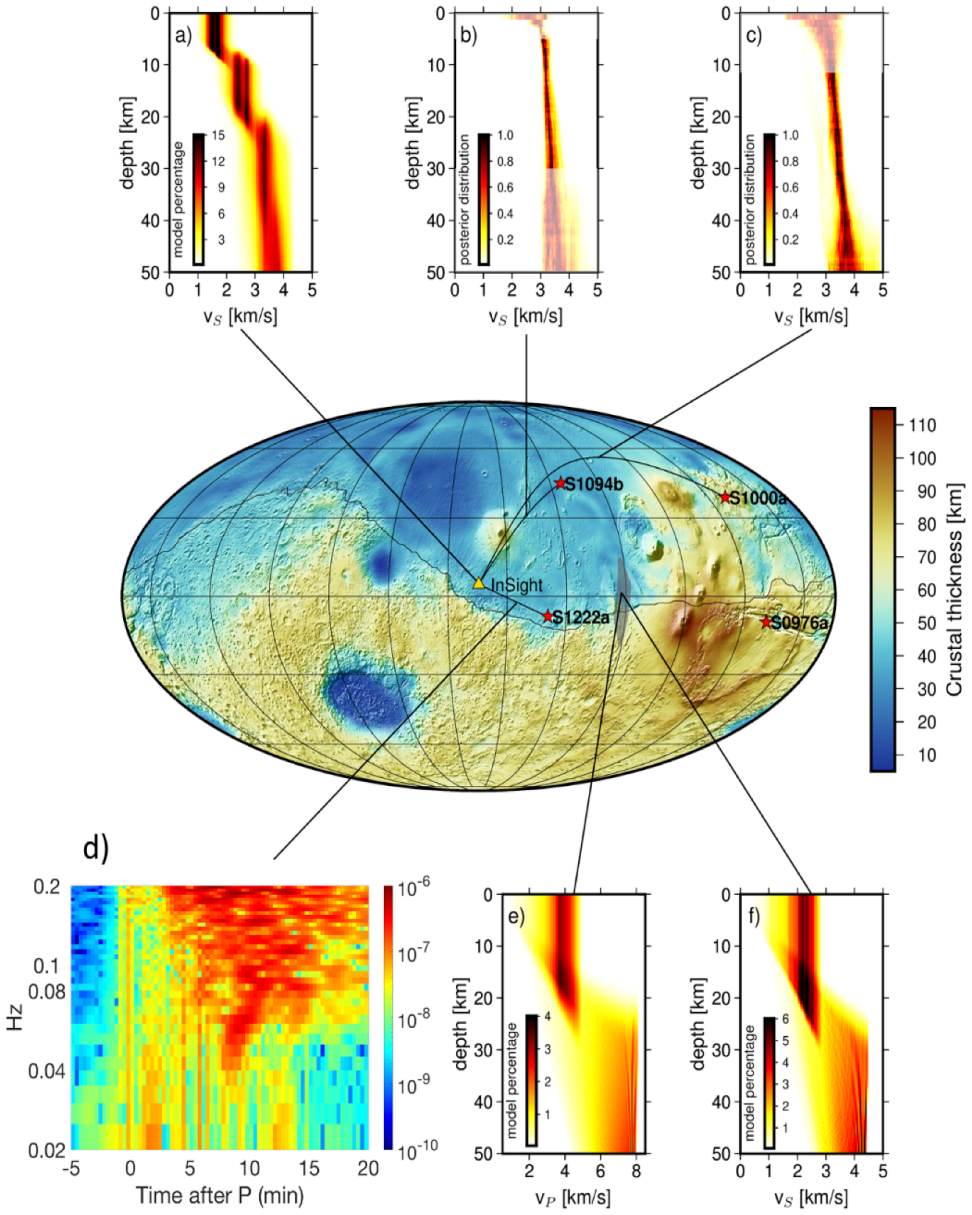

Figure 12: Map of the global crustal thickness of Mars, based on the seismic measurements beneath the InSight lander and orbital gravity and topography measurements (Wieczorek et al. 2022). The map is based on a crustal thickness of 39 km beneath InSight, a uniform crustal density of 2900 kg/m³ and mantle and core densities from Khan et al. (2022). The outline of the dichotomy boundary is taken from Andrews-Hanna et al. (2008), and the topographic relief from the Mars Orbiter Laser Altimeter (Smith et al. 2001). Insets show modes based on specific seismic measurements and the locations they refer to: a) S-wave velocities beneath the InSight lander (Knapmeyer-Endrun et al. 2021) b) S-wave velocities along the raypath between S1094b and the lander. Shaded areas are not well resolved (Kim et al. 2022) c) S-wave velocities along the raypath between S1000a and the lander. Shaded areas are not well resolved (Kim et al. 2022) d) S1222a surface waves spectrograms for the first 20 minutes of the VBBZ signal, for 200 sec windows with clear dispersion pattern of the surface waves. Structure inversions are in progress (Beghein et al. 2022, Xu et al. 2022) e) and f) P- and S-wave velocities at S0986a bounce point, shaded in gray on the map (Li et al. 2022c)

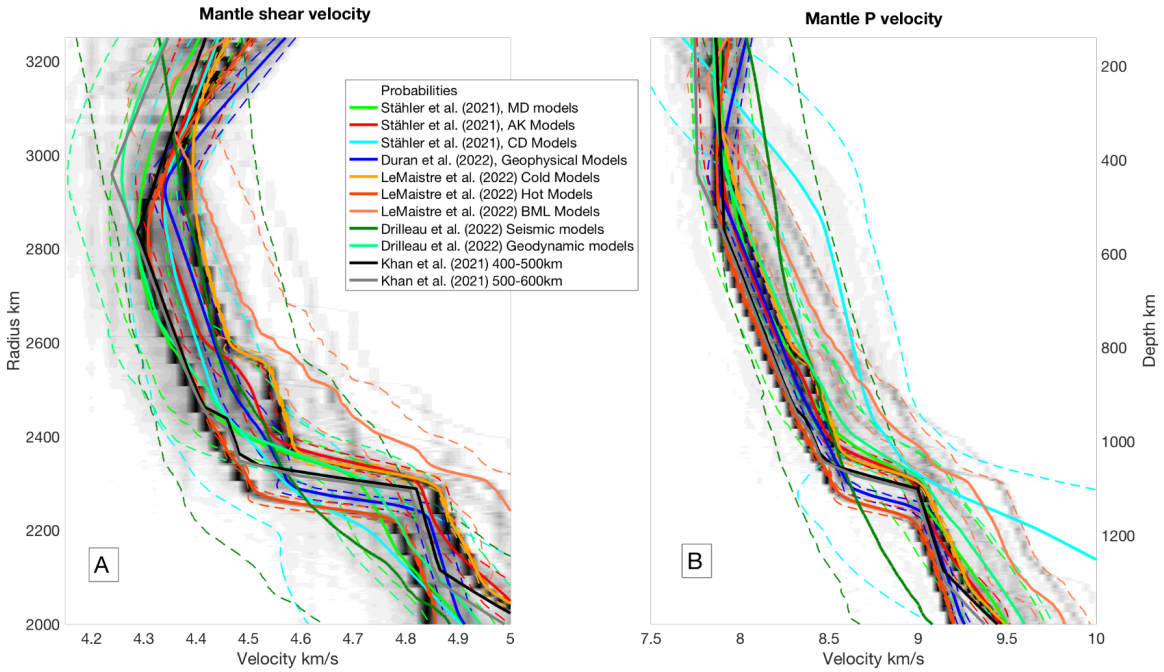

Figure 13: Compilation of the different mantle models obtained from joint inversions of direct (P,S) and secondary phases (PP, PPP, SS, SSS, ScS). From left to right for (A) seismic shear-wave velocities v_s, (B) seismic compressional-wave velocities v_p. Radius is on the left and depth is on the right, both in km. Model references are provided in the legend of figure (A), with the same color codes in A and B. For each family of models, the solid line provides the mean model, while the dashed lines provide the 1-σ uncertainty. The gray background represents the a-posteriori dispersion of these models, in terms of probability, assuming that each family of models has the same probability. Note that below 800 km depth (2600 km radius), no P wave travel time constraints directly the P-wave velocity profiles. The latter are therefore indirectly constrained by ScS travel times, by vp/vs ratio from models of mineralogy and temperature and by depth correlations with v_p profiles above 800 km. Resolution in the mantle transition zone, for radius smaller than 2400 km, is also poor for S-waves, as shown by the larger dispersion of the published models.

References

Anderson DL, Miller WF, Latham GV, Nakamura Y, Toksöz MN et al. 1977. Seismology on Mars. J. Geophys. Res. **82**:4524–46, doi: 10.1029/JS082i028p04524

Andrews-Hanna J, Zuber M & Banerdt WB 2008. The Borealis basin and the origin of the martian crustal dichotomy. *Nature* **453:** 212–1215, doi : 10.1038/nature07011

Banerdt WB, Smrekar S, Banfield D, Giardini D, Golombek M et al. 2020. Initial results from the InSight mission on Mars, *Nature Geoscience* **13**, 183-189, doi: 10.1038/s41561-020-0544-y

Banfield D, Spiga A, Newman C, Forget F, Lemmon M et al. 2020. The atmosphere of Mars as observed by InSight, *Nature Geoscience* **13**:190-198, doi: 10.1038/s41561-020-0534-0

Banfield D., Rodriguez-Manfredi JA., Russell CT, Rowe KM, Leneman Det al. 2019. InSight Auxiliary Payload Sensor Suite (APSS), *Space Sci Rev* **215**:4, doi: 1007/s11214-018-0570-x

Barkaoui S, Lognonné P, Kawamura T, Stutzmann E, Seydoux L et al. (2021), Anatomy of streaming Mars SEIS data from unsupervised learning, *Bull. Seism. Soc. America* **111**: 2964–2981, doi: 10.1785/0120210095

Bates JR, Lauderdale WW and Kernaghan H 1979. ALSEP Termination report, NASA reference publication 1036, https://www.lpi.usra.edu/lunar/ALSEP/pdf/NASA%20RP-1036.pdf

Beghein C, Li J, Maguire R, Wookey J et al. 2022. Constraining Seismic Anisotropy on Mars: New Challenges and First Detection, AGU Fall Meeting, **ID# 1078565** .

Bell JF, Wolff MJ, Malin MC, Calvin WM, Cantor BA et al. (2009). Mars Reconnaissance Orbiter Mars Color Imager (MARCI): Instrument description, calibration, and performance, *J. Geophys. Res.*, **114**:E08S92, doi:10.1029/2008JE003315

Böse M, Giardini D, Stähler S, Ceylan S, Clinton JF et al. 2018, Magnitude Scales for Marsquakes, Magnitude Scales for Marsquakes, *Bull. Seis. Soc. America*, **108**:2764–2777, doi: 10.1785/0120180037

Böse MD, Clinton JF, Ceylan S, Euchner F, van Driel M et al. 2017. Probabilistic Framework for Single-Station Location of Seismicity on Earth and Mars, *Physics of the Earth and Planetary Interiors*, **262**:48-65, doi: 10.1016/j.pepi.2016.11.003

Böse MD, Stähler SC, Deichmann N, Giardini D, Clinton JF et al. 2021. Magnitude Scales for Marsquakes Calibrated from InSight Data, Bull. Seism. Soc. America, **111**:3003–3015, doi: 10.1785/0120210045

Bozdag E., Ruan Y, Metthez N, Khan A, Leng K et al. 2017. Simulations of seismic wave propagation on Mars, *Space Sci Rev*, **211**:571-594, doi: 10.1007/s11214-017-0350-z

Brinkman N, Stähler SC , Giardini D, Schmelzbach C, Khan A et al. 2021. First focal mechanisms of marsquakes, *J. Geophys. Res: Planet.*, **126**:e2020JE006546, doi: 10.1029/2020JE006546

Brinkman N, Schmelzbach C, Sollberger D, van Driel M, ten Pierick J et al. 2019. The first active seismic experiment on Mars to characterize the shallow subsurface structure at the InSight landing site, SEG Technical Program Expanded Abstracts 2019, 4756-4760, doi: 10.1190/segam2019-3215661.1

Brinkman N, Schmelzbach C, Sollberger D, ten Pierick J et al 2022, In-situ regolith seismic velocity measurement at the InSight landing site on Mars, in revision, J. Geophys. Res. Planet, doi: 10.1002/essoar.10512064.1.

Carrasco S, Knapmeyer-Endrun B, Margerin L, Schmelzbach C, Onodera K et al. 2022,

Empirical H/V spectral ratios at the InSight landing site and implications for the Martian subsurface structure, in revision, J. Geophys. Int.
Ceylan S, Clinton JF, Giardini D, Böse M, Charalambous C et al. 2020. Companion guide to the Marsquake Catalog from InSight, Sols 0-478: data content and non-seismic events, *Physic. Planet. Earth*. Int, **310**:106597 doi: 10.1016/j.pepi.2020.106597,
Ceylan S, Clinton JF, Giardini D, Stähler SC, Horleston A et al. 2022. The marsquake catalogue from InSight, sols 0–1011, *Phys. Earth Planet. Inter.*, in review, doi: 10.1002/essoar.10512032.1.
Charalambous C, Stott AE, Pike WT, McClean JB, Warren T et al. 2021, A Comodulation Analysis of Atmospheric Energy Injection into the Ground Motion at InSight, Mars, *J. Geophys. Res.: Planet*, **126**:e2020JE006538, doi: 10.1029/2020JE006538
Clinton J, Giardini D, Böse M, Ceylan S, van Driel M et al. 2018. The Marsquake Service : Securing Daily Analysis of SEIS Data and Building the Martian Seismicity Catalogue for InSight, Space Sci Rev, **214**:133, doi: 10.1007/s11214-018-0567-5
Clinton J, Ceylan S, van Driel M , Giardini D, Stähler SC et al. 2021. The Marsquake Catalog from InSight, Sols 0-478: data content and non-seismic events, *Physic. Planet. Earth. Int.*, **310**:106595, doi: 10.1016/j.pepi.2020.106595,
Clinton JF., Giardini D, Lognonné P, Banerdt WB, van Driel M et al. 2017. Preparing for InSight: An Invitation to Participate in a Blind Test for Martian Seismicity, *Seismological Research Letters*, **88**:1290–1302, doi : 10.1785/0220170094
Collins GS, Newland EL, Schwarz D, Coleman M, McMullan S et al. 2022. Meteoroid fragmentation in the martian atmosphere and the formation of crater clusters. *J. Geophys. Res.: Planets*, **127**:e2021JE007149, doi: 10.1029/2021JE007149
Compaire N, Margerin L, Monnereau M, Garcia RF, Lange L et al. 2022. Seasonal variations of subsurface seismic velocities monitored by the SEIS-InSight seismometer on Mars, *Geophysical Journal International*, **229**:776–799, doi: 10.1093/gji/ggab499
Compaire N, Margerin L, Garcia RF, Pinot B, Calvet M et al. 2021. Autocorrelation of the ground vibrations recorded by the SEIS-InSight seismometer on Mars, *J. Geophys. Res.: Planets*, **126**:e2020JE006498, doi: 10.1029/2020JE006498
da Silva S and Corso G 2021. Nonextensive Gutenberg-Richter law and the connection between earthquakes and marsquakes. *European Physical Journal B*, **94**:25, doi: 10.1140/epjb/s10051-020-00015-5.
Dahmen NL, Zenhäusern G, Clinton JF, Giardini D, Stähler SC et al. 2021, Resonances and Lander Modes observed by InSight on Mars (1-9 Hz), Bull. Seism. Soc. America, **111**:2924–2950, doi: 10.1785/0120210056
Dahmen NL, Clinton JF, Meier M-A., Stähler SC, Kim D. et al. 2022. A Deep Marsquake Catalogue, submitted to *J. Geophys. Res. Planet.,* doi: 10.1002/essoar.10512017.1
Dahmen NL, Clinton JF, Ceylan S, van Driel M, Giardini D et al. 2020, Super high frequency events: a new class of events recorded by the InSight seismometers on Mars, *J. Geophys. Res.: Planets*, **126**:e2020JE006599, doi: 10.1029/2020JE006599
Daubar IJ, Lognonné P, Teanby NA, Collins GS, Clinton JF et al. 2020. A New Crater Near InSight: Implications for Seismic Impact Detectability on Mars. *J. Geophys. Res.: Planets*, **125**:e2020JE006382, doi: 10.1029/2020JE006382
Daubar IJ, Lognonné P, Teanby NA, Miljkovic K, Stevanović Jet al. 2018. Impact-Seismic Investigations of the InSight Mission, *Space Sci Rev*, **214**:132, doi: 10.1007/s11214-018-0562-x
Deng S & Levander A 2020. Autocorrelation reflectivity of Mars. *Geophys. Res. Lett.*, **47**:e2020GL089630, doi: https://doi.org/10.1029/2020GL089630
Drilleau M, Samuel H, Garcia RF, Rivoldini A, Perrin C et al. 2022. Marsquake locations and 1-D seismic models for Mars from InSight data, in press, *J. Geophys. Res.: Planet*, doi:

10.1002/essoar.10511074.2
Drilleau M, Samuel H, Rivoldini A, Panning M, Lognonné P 2021. Bayesian inversion of the Martian structure using geodynamic constraints, *Geophysical Journal International*, **226**:1615–1644, doi: 10.1093/gji/ggab105
Durán C, Khan A, Ceylan S, Zenhäusern G, Stähler S et al. 2022. Seismology on Mars: An analysis of direct, reflected, and converted seismic body waves with implications for interior structure, Physics of the Earth and Planetary Interiors, **325**:106851, doi: 10.1016/j.pepi.2022.106851.
Fayon L, Knapmeyer-Endrun B, Lognonné P, Bierwirth M, Kramer A et al 2018. A numerical model of the SEIS leveling system transfer matrix and resonances: application to SEIS rotational seismology and dynamic ground interaction, *Space Science Review*, **214**:119, doi:10.1007/s11214-018-0555-9
Fernando B, Wójcicka N, Han Z, Stott A, Ceylan S et al. 2021. Questions to Heaven, *Astronomy & Geophysics*, **62**: 6.22–6.25, doi: 10.1093/astrogeo/atab103
Fernando B, Wójcicka N, Maguire R, Stähler S, Stott AE et al. 2021 Seismic constraints from a Mars impact experiment using InSight and Perseverance. *Nat Astron, **6**:59-64,* doi: 10.1038/s41550-021-01502-0
Folkner WM, Dehant V, Le Maistre S, Yseboodt M, Rivoldini T et al. 2018. The Rotation and Interior Structure Experiment on the InSight Mission to Mars. *Space Sci Rev,* **214:**100, doi: 10.1007/s11214-018-0530-5
Garcia RF, Murdoch N, Lorenz R, Spiga A, Bowman DC et al. 2021, Search for infrasound signals in InSight data using coupled pressure/ground deformation methods, *Bull. Seism. Soc. America*, **111**:3055–3064, doi: 10.1785/0120210079
Garcia RF, Kenda B, Kawamura T, Spiga A, Murdoch N et al. 2020. Pressure effects on the SEIS-InSight instrument, improvement of seismic records, and characterization of long period atmospheric waves from ground displacements, *J. Geophys. Res.: Planets*, **125**:e2019JE006278, doi: 10.1029/2019JE006278
Garcia RF, Brissaud Q, Rolland L, Martin R, Komatitsch D et al. 2017. Finite-Difference Modeling of Acoustic and Gravity Wave Propagation in Mars Atmosphere: Application to Infrasounds Emitted by Meteor Impacts, *Space Sci Rev*, **211**:547-570, doi:10.1007/s11214-016-0324-6
Garcia RF, Daubar IJ, Beucler E, Posiolova L, Collins GS et al. 2022. Seismological Location and Orbital Imaging of Newly Formed Craters on Mars, in press, Nature Geoscience.
Giardini D, Lognonné P, Banerdt WB, Pike WT, Christensen U et al. 2020. The Seismicity of Mars, *Nature Geoscience*, **13**:205-212, doi: 10.1038/s41561-020-0539-8
Golombek M, Warner N, Grant J, Hauber E, Ansan V et al 2020. Geology of the InSight Landing Site on Mars, *Nature communication*, **11**:1014, doi: 10.1038/s41467-020-14679-1
Gudkova T, Lognonné P, Gagnepain-Beyneix J 2011. Seismic source inversion for Large impacts detected by the Apollo seismometers, *Icarus*, **211**:1049-1065, doi: 10.1016/j.icarus.2010.10.028
Gudkova T, Lognonné P, Miljković K, Gagnepain-Beyneix J 2015. Impact cutoff frequency - momentum scaling law inverted from Apollo seismic data, *Earth and Planetary Science Letters*, **427**:57-65., doi: 10.1016/j.epsl.2015.06.037
Harada Y 2022. Reconsideration of the anelasticity parameters of the martian mantle: Preliminary estimates based on the latest geodetic parameters and seismic models, *Icarus*, **383**:114917, doi: 10.1016/j.icarus.2022.114917
Heap MJ 2019. P- and S-wave velocity of dry, water-saturated, and frozen basalt: Implications for the interpretation of Martian seismic data. *Icarus*, **330**:11–15, doi: 10.1016/j.icarus.2019.04.020
Hobiger M, Hallo M, Schmelzbach C, Stähler SC, Fäh D et al. 2021. The shallow structure of

Mars at the InSight landing site from inversion of ambient vibrations. *Nat Commun* **12**:6756, doi: 10.1038/s41467-021-26957-7
Horleston A, Clinton JF, Ceylan S, Giardini D, Charalambous C et al. 2022. The Far Side of Mars: Two Distant Marsquakes Detected by InSight. *The Seismic Record*, **2**:88, doi: 10.1785/0320220007
Hurst KJ, Ervin J, Fayon L, Kedar S, Knapmeyer-Endrun B et al. 2021, Resonances of the InSight Seismometer on Mars, Bull. Seism. Soc. America, **111**:2951–2963, doi: 10.1785/0120210137
InSight Mars SEIS Data Service 2019. SEIS raw data, Insight Mission. IPGP, JPL, CNES, ETHZ, ICL, MPS, ISAE-Supaero, LPG, MFSC, doi: 10.18715/SEIS.INSIGHT.XB_2016
InSight Marsquake Service 2020. Mars Seismic Catalogue, InSight Mission; V1 2/1/2020. ETHZ, IPGP, JPL, ICL, ISAE-Supaero, MPS, Univ. Bristol, doi: 10.12686/a6
InSight Marsquake Service 2022. Mars Seismic Catalogue, InSight Mission; V11 2022-07-01. ETHZ, IPGP, JPL, ICL, Univ. Bristol, doi: 10.12686/a17
Irving J, Antonangeli D, Beghein C, Drilleau M, Garcia RF et al. 2022. First observations of seismic waves travelling through the Martian core, AGU Fall Meeting 2022, **ID# 1067574**
Jacob A, Plasman M, Perrin C, Fuji N, Lognonné P et al. 2022. Seismic sources of InSight marsquakes and seismotectonic context of Elysium Planitia, Mars, *Tectonophysics*, 837:229434, doi: 10.1016/j.tecto.2022.229434
Joshi R, Knapmeyer-Endrun B, Mosegaard K, Igel R, Christensen UR, Lognonné P 2022. Joint Inversion of receiver functions and apparent incidence angles to determine the crustal structure of Mars, submitted to *Geophys. Res. Lett*, doi: 10.1002/essoar.10512135.1
Karakostas F, Schmerr N, Maguire R, Huang Q, Kim D et al. 2021. Scattering Attenuation of the Martian Interior through Coda Wave Analysis, *Bull. Seism. Soc. America*, **111**:3035–3054, doi: 10.1785/0120210253
Kawamura T, Clinton JF, Zenhäusern G, Ceylan S, Horleston AC et al. 2022. Largest Marsquake Ever Detected by InSight: S1222a, submitted to *Geophys. Res. Lett.*
Kedar S, Andrade J, Banerdt WB, Delage P, Golombek M et al. 2017. Analysis of Regolith Properties Using Seismic Signals Generated by InSight's HP3 Penetrator, *Space Sci Rev*, **211**:315, doi: 10.1007/s11214-017-0391-3
Kedar S, Panning MP, Smrekar SE, Stähler SC, King SD et al. 2021. Analyzing low frequency seismic events at Cerberus Fossae as long period volcanic quakes, *J. Geophys. Res.: Planets*, **126**:e2020JE006518, doi: 10.1029/2020JE006518
Kenda B, Drilleau M, Garcia RF, Kawamura T, Murdoch N et al. 2020. Subsurface structure at the InSight landing site from compliance measurements by seismic and meteorological experiments, *J. Geophys. Res.: Planets*, **125**:e2020JE006387, doi: 10.1029/2020JE006387
Kenda B, Lognonné P, Spiga A, Kawamura T, Kedar S et al. 2017. Modeling of ground deformation and shallow surface waves generated by Martian dust, devils and perspectives for near-surface structure inversion, Space Science review, **211**:501-524, doi: 10.1007/s11214-017-0378-0.
Khan A, Ceylan S, van Driel M, Giardini D, Lognonné P et al. 2021: Imaging the upper mantle structure of Mars with InSight seismic data, *Science*, **373**:434-438, doi: 10.1126/science.abf2966
Khan A, van Driel M, Böse M, Giardini D, Ceylan S et al. 2016. Single-station and single-event marsquake location and inversion for structure using synthetic Martian waveforms, *Physics of the Earth and Planetary Interiors*, **258**:28-42, doi: 10.1016/j.pepi.2016.05.017
Khan A, Sossi PA, Liebske C, Rivoldini A, Giardini D 2022. Geophysical and cosmochemical evidence for a volatile-rich Mars, Earth and Planetary Science Letters, **578**:117330, doi: 10.1016/j.epsl.2021.117330
Kim D, Lekić V, Irving JCE, Schmerr N, Knapmeyer-Endrun B et al. 2021. Improving

constraints on planetary interiors with PPs receiver functions. *J. Geophys. Res.: Planets*, **126**:e2021JE006983. doi: 10.1029/2021JE006983
Kim D, Davis P, Lekić V, Maguire R, Compaire N et al. 2021. Potential Pitfalls in the Analysis and Structural Interpretation of Mars' Seismic Data from InSight, *Bull. Seism. Soc. America*, **111**:2982–3002., doi: 10.1785/0120210123
Kim D, Banerdt WB, Ceylan S, Giardini D, Lekic V et al. 2022. Surface Waves and Crustal Structure on Mars, in revision, Science.
Knapmeyer-Endrun B, Panning MP, Bissig F, Joshi R, Khan A et al. 2021. Thickness and structure of the Martian crust from InSight seismic data, Science, **373**:438-443, doi: 10.1126/science.abf89662021
Knapmeyer-Endrun B, Murdoch N, Kenda B, Golombek MP, Knapmeyer M et al. 2018. Influence of Body Waves, Instrumentation Resonances, and Prior Assumptions on Rayleigh Wave Ellipticity Inversion for Shallow Structure at the InSight Landing Site, *Space Science Review*, **214**:94, doi: 10.1007/s11214-018-0529-y
Knapmeyer M, Stähler SC, Daubar I, Forget F, Spiga A et al. 2021, Seasonal seismic activity on Mars, *Earth and Planetary Science Letters*, **576**:117171, doi: 10.1016/j.epsl.2021.117171
Knapmeyer M, Knapmeyer-Endrun B, Plesa AC, Böse M, Kawamura T et al. 2019. Estimation of the Seismic Moment Rate from an Incomplete Seismicity Catalog, in the Context of the InSight Mission to Mars, *Bull. Seis. Soc. America*, **109**:1125–1147, doi: 10.1785/0120180258
Le Maistre S, Rivoldini A, Caldiero A, Yseboodt M, Baland RM et al. 2022, Spin state and deep interior structure of Mars from InSight radio tracking, in revision, *Science*
Li J, Beghein C, Wookey J, Davis P, Lognonné P et al. 2022. Evidence for Crustal Seismic Anisotropy at the InSight Lander Site, *Earth. Planet. Science. Lett.*, **593**:117654, doi: 10.1016/j.epsl.2022.117654
Li J, Beghein C, Davis P, Lognonné P, Kim D et al. 2022, Detection of SV- to P-wave Reflections on Mars and Consequences for Crustal Structure, in revision, *Earth and Space Science*, doi: 10.1002/essoar.10512137.1
Li J, Beghein C, McLennan SM, Horleston AC, Huang Q et al. 2022. Second Seismic Anchor Point of the Martian Crustal Structure Away From the InSight Landing Site, submitted to *Nature communication*, doi: 10.21203/rs.3.rs-1829147/v1
Li J, Beghein C, Panning M, Davis P, Lognonné P and Banerdt WB 2022. New Constraints on the Martian Crustal Structure and Seismic Anisotropy near the Dichotomy Revealed by the Largest Marsquake Ever Recorded, AGU Fall Meeting 2022, **ID# 1078651**
Lognonné P & Mosser B 1993. Planetary Seismology, **14**:239-302, *Survey in Geophysic*, doi: 10.1007/BF00690946
Lognonné P, Le Feuvre M, Johnson CL, and Weber RC 2009. Moon meteoritic seismic hum: steady state prediction, *J. Geophys. Res.*, **114**:E12003, doi:10.1029/2008JE003294.
Lognonné P. and Johnson CL 2015. 10.03 - Planetary Seismology, In Treatise on Geophysics (Second Edition), edited by Gerald Schubert, Elsevier, Oxford, Pages 65-120, ISBN 9780444538031, doi: 10.1016/B978-0-444-53802-4.00167-6
Lognonné P, Banerdt WB, Giardini D, Pike WT, Christensen U et al., SEIS: Insight's Seismic Experiment for Internal Structure of Mars, *Space Sci Rev*, **215**:12, doi: 10.1007/s11214-018-0574-6
Lognonné P, Karakostas F, Rolland L and Y. Nishikawa Y 2016. Modeling of atmospheric-coupled Rayleigh waves on planets with atmosphere: From Earth observation to Mars and Venus perspectives, *Journal of the Acoustical Society of America*, **140**:1447-1468, doi: 10.1121/1.4960788
Lognonné P 2005. Planetary seismology, *Annual Review in Earth Planet. Sci.,* **33** :19.1-19.34, doi:10.1146/annurev.earth.33.092203.122605
Lognonné P, Banerdt WB, Pike WT, Giardini D, Christensen U et al. 2020. Constraints on the

shallow elastic and anelastic structure of Mars from InSight seismic data, *Nature geoscience*, **13**:213-220, doi: 10.1038/s41561-020-0536-y
Lognonné P, Schimmel M, Stutzmann E, Drilleau M, Samuel H et al. 2022. Martian free oscillations: Search in SEIS data and implications, Europlanet Science Congress 2022, Granada, Spain, 18–23 Sep 2022, EPSC2022-738
Lorenz RD, Kedar S, Murdoch N, Lognonné P, Kawamura T et al. 2015. Seismometer Detection of Dust Devil Vortices by Ground Tilt, *Bull. Seis. Soc. America*, **105**:3015-3023, doi: 10.1785/0120150133
Lorenz RD, Spiga A, Lognonné P, Plasman M, Newman CE and Charalambous C 2021. The whirlwinds of Elysium: A catalog and meteorological characteristics of "dust devil" vortices observed by InSight on Mars, *Icarus*, **355**:114119, doi: 10.1016/j.icarus.2020.114119.
Lucas A, Bourdon L, Mangeney A, Sainton G, Bah MA et al. 2022. InSight for seismically detectability and seismically triggered avalanches on Mars, Europlanet Science Congress 2022, Granada, Spain, 18–23 Sep 2022, EPSC2022-366
Mahvelati S and Coe TJ 2021. Horizontal-to-Vertical Spectral Ratio (HVSR) Analysis of the Martian Passive Seismic Data from the InSight Mission. Paper presented at the 17th Biennial International Conference on Engineering, Science, Construction, and Operations in Challenging Environments: Space Exploration, Utilization, Engineering, and Construction in Extreme Environments, Earth and Space 2021, April 19, 2021 - April 23, 2021, Seattle, WA, United states doi: 10.1061/9780784483374.011
Maki JN, Golombek M, Deen R, Abarca H, Sorice C et al. 2018. The Color Cameras on the InSight Lander. *Space Sci Rev* **214**:105, doi: 10.1007/s11214-018-0536-z
Manga M. and Wright V 2021. No Cryosphere-Confined Aquifer Below InSight on Mars. *Geophys. Res. Lett.*, **48**:e2021GL093127, doi: 10.1029/2021gl093127
Martire L, Garcia RF, Rolland L, Spiga A, Lognonné P et al. 2020. Martian infrasound: Numerical modeling and analysis of insight's data, *J. Geophys. Res.: Planets*, **125**:e2020JE006376, doi: 10.1029/2020JE006376
Menina S, Margerin L, Kawamura T, Lognonné P, Marti J et al. 2021, Energy envelope and attenuation characteristics of High Frequency (HF) and Very High Frequency (VF) Martian events, *Bull. Seism. Soc. America*, **111**:3016–3034, doi: 10.1785/0120210127
Millour E, Forget F, Gonzalez-Galindo F, Spiga A, Lebonnois S et al. 2018. The Mars Climate Database (version 5.3). Sae technical paper series 2
Mimoun D, Murdoch N, Lognonné P, Hurst K, Pike WT et al. 2017. The Noise Model of the SEIS Seismometer of the InSight Mission to Mars, *Space Science review*, **211**:383–428, doi: 10.1007/s11214- 017-0409-x
Morgan P, Grott M, Knapmeyer-Endrun B, Golombek M, Delage P et al. 2018. A Pre-Landing Assessment of Regolith Properties at the InSight Landing Site, *Space Sci Rev*, **214**: 104, doi: 10.1007/s11214-018-0537-y
Murdoch N, Spiga A, Lorenz R, Garcia RF, Perrin C et al. 2021. Constraining Martian regolith and vortex parameters from combined seismic and meteorological measurements, *J. Geophys. Res: Planets*, **126**:e2020JE006410, doi: 10.1029/2020JE006410
Murdoch N, Kenda B, Kawamura T, Spiga A, Lognonné P et al. 2017a, Estimations of the seismic pressure noise on Mars determined from Large Eddy Simulations and demonstration of pressure decorrelation techniques for the InSight mission, *Space Science review*, **211**:457-483, doi: 10.1007/s11214-017-0343-y
Murdoch N, Mimoun D, Garcia RF, Rapin W, Kawamura T et al. 2017b., Evaluating the Wind-Induced Mechanical Noise on the InSight Seismometers, *Space Science Review*, **211**:429-455, doi:10.1007/s11214-016-0311-y
Nakamura Y, Anderson DL. 1979. Martian wind activity detected by a seismometer at Viking lander 2 site. *Geophys. Res. Lett.* 6: 499–502, doi: 10.1029/GL006i006p00499

Nishikawa Y, Lognonné P, Kawamura T, Spiga A, Stutzmann E et al., Mars' Background Free Oscillations , Space Sci Rev, 215:13, doi: 10.1007/s11214-019-0579-9
Onodera K 2022, Subsurface structure of the Moon and Mars from 3D seismic wave propagation simulation and analysis of Apollo and InSight seismic data, Doctoral dissertation of The Graduate University for Advanced Studies, SOKENDAI and Université Paris Cité https://ir.soken.ac.jp/?action=repository_uri&item_id=6507&file_id=19&file_no=2
Ortiz HD, Matoza RS and Tanimoto T 2022. Autocorrelation infrasound interferometry on Mars. *Geophys. Res. Lett.*, 49:e2021GL096225, doi: 10.1029/2021GL096225
Panning MP, Pike WT, Lognonné P, Banerdt WB, Murdoch N et al. 2020. On-deck seismology: Lessons from InSight for future planetary seismology. *J. Geophys. Res.: Planets*, **125**:e2019JE006353, doi: 10.1029/2019JE006353
Panning MP, Beucler E, Drilleau M, Mocquet A, Lognonné P, Banerdt WB 2015. Verifying single-station seismic approaches using Earth-based data: Preparation for data return from the InSight mission to Mars, *Icarus*, **248**:230-242, doi: 10.1016/j.icarus.2014.10.035
Panning MP, Lognonné P, Banerdt WB, Garcia R, Golombek M et al. 2017. Planned products of the Mars Structure Service for the InSight mission, Mars, *Space Science review*, **211**:611–650, doi: 10.1007/s11214-016-0317-5
Panning MP, Banerdt WB, Beghein C, Ceylan S, Clinton JF et al. 2022. Locating the largest event observed on Mars with multi-orbit surface waves, AGU Fall meeting, ID# 1110761
Peterson J 1993. Observation and modeling of seismic background noise. U.S. Geological Survey Open-File Report, 93-322, pp. 1–45, doi: 10.3133/ofr93322
Perrin C, Jacob A, Lucas A, Myhill R, Hauber E et al. 2022. Geometry and segmentation of Cerberus Fossae, Mars: implications for marsquake properties., *J. Geophys*, **127**:e2021JE007118, doi: 10.1029/2021JE007118
Perrin C, Rodriguez S, Jacob A, Lucas A, Spiga A et al. 2020. Monitoring of dust devil tracks around the InSight landing site, Mars, and comparison with in situ atmospheric data, *Geophys. Res. Lett.*, **47**:e2020GL087234, doi: 10.1029/2020GL087234
Plesa AC, Knapmeyer M, Golombek MP, Breuer D, Grott M et al. 2018. Present-day Mars' Seismicity Predicted from 3-D Thermal Evolution Models of Interior Dynamics, *Geophys. Res. Lett.*, **45**:2580–2589, doi: 10.1002/2017GL076124
Posiolova LV, Lognonné P, Banerdt WB, Clinton JF, Collins GS et al. 2022. Large hypervelocity impact on Mars co-located by orbital imaging and surface seismic recording, in revision, Science, 2022.
Pou L, Nimmo F, Lognonné P, Mimoun D, Garcia RF et al. 2021. Forward Modeling of the Phobos Tides and applications to the first Martian year of the InSight mission. *Earth and Space Science*, **8**:e2021EA001669, doi: 10.1029/2021EA001669.
Rivas-Dorado S, Ruíz J, Romeo I 2022. Giant dikes and dike-induced seismicity in a weak crust underneath Cerberus Fossae, Mars, *Earth and Planetary Science Letters*, **594**:117692, doi: 10.1016/j.epsl.2022.117692
Ringler AT, Anthony RE, Aster RC, Ammon CJ, Arrowsmith S et al. 2022. Achievements and Prospects of Global Broadband Seismographic Networks after 30 Years of Continuous Geophysical Observations, *Reviews of Geophysics*, **60**:e2021RG000749, doi: 10.1029/2021RG000749
Samuel H, Ballmer MD, Padovan S, Tosi N, Rivoldini A and Plesa AC (2021). The thermo-chemical evolution of Mars with a strongly stratified mantle. *J. Geophys. Res.: Planets*, **126**:e2020JE006613, doi: 10.1029/2020JE006613
Savoie D, Richard A, Goutaudier M, Lognonné P, Hurst K et al. 2021. Finding SEIS North on Mars: Comparisons between SEIS sundial, Inertial and Imaging measurements and consequences for seismic analysis, *Earth and Space Science*, **8**:e2020EA001286, doi: 10.1029/2020EA001286

Schimmel M, Stutzmann E, Lognonné P, Compaire N, Davis P et al. 2021. Seismic noise autocorrelations on Mars. *Earth and Space Science*, **8**:e2021EA001755, doi: 10.1029/2021EA001755
Scholz JR, Widmer-Schnidrig R, Davis P, Lognonné P, Pinot B et al. 2020, Detection, Analysis, and Removal of Glitches From InSight's Seismic Data From Mars, *Earth and Space Science*, **7**:e2020EA001317, doi: 10.1029/2020EA001317,
Smith DE, Zuber MT, Frey HV, Garvin JB, Head JW et al. 2001. Mars Orbiter Laser Altimeter: Experiment summary after the first year of global mapping of Mars, *J. Geophys. Res.: Planets*, **106**:23689–23722, doi: 10.1029/2000JE001364
Smrekar SE, Lognonné P, Spohn T, Banerdt WB, Breuer, D et al. 2019. Pre-mission InSights on the Interior of Mars, *Space Sci Rev*, **215**:3, doi: 10.1007/s11214-018-0563-9
Sollberger D, Schmelzbach C, Andersson F, Robertsson JOA, Brinkman N et al. 2021. A reconstruction algorithm for temporally aliased seismic signals recorded by the InSight Mars lander. *Earth and Space Science*, **8**:e2020EA001234, doi: 10.1029/2020EA001234
Spohn T, Grott M, Smrekar SE, Knollenberg J, Hudson TL et al. 2018. The Heat Flow and Physical Properties Package (HP^3) for the InSight Mission. *Space Sci Rev*, **214:**96 doi: 10.1007/s11214-018-0531-4
Stähler SC, Widmer-Schnidrig R, Scholz JR, van Driel M, Mittelholz A et al. 2020. Geophysical observations of Phobos transits by InSight, *Geophys. Res. Lett.*, **47**:e2020GL089099 doi: 10.1029/2020GL089099
Stähler SC, Khan A, Banerdt WB, Lognonné P, Giardini D et al. 2021. Seismic detection of the martian core, *Science,* **373**:443-448, doi: 10.1126/science.abi7730
Stähler SC, Mittelholz A, Perrin C, Kawamura T, Kim D et al. 2022. Tectonics of Cerberus Fossae unveiled by marsquakes, in revision, Nature Astronomy, doi: 10.48550/arXiv.2206.15136
Stähler SC, Panning MP, Antonangeli D, Banerdt WB, Banfield D et al. 2022. A Cerberus Fossae Seismic Network, Low-Cost Science Mission Concepts for Mars Exploration, held 29-31 March, 2022 in Pasadena, California. LPI Contribution No. 2655, id.5024
Stevanović J, Teanby NA, Wookey J, Selby N, Daubar IJ *et al.* 2017. Bolide Airbursts as a Seismic Source for the 2018 Mars InSight Mission, *Space Sci Rev*, **211:**525–545, doi: 10.1007/s11214-016-0327-3
Stott A, Garcia RF, Chédozeau A, Spiga A, Murdoch N et al. 2022. Using machine learning to separate atmospherically generated noise from marsquakes, Europlanet Science Congress 2022, Granada, Spain, 18–23 Sep 2022, EPSC2022-833.
Stutzmann E, Schimmel M, Lognonné P, Horleston AC, Ceylan S et al. 2020. Polarized ambient noise on Mars, *J. Geophys. Res.: Planets*, **125**:e2020JE006545, doi: 10.1029/2020JE006545
Suemoto Y, Ikeda T & Tsuji T 2020. Temporal variation and frequency dependence of seismic ambient noise on Mars from polarization analysis. *Geophys. Res. Lett.*, **47**:e2020GL087123, doi: 10.1029/2020GL087123
Sun W, Tkalčić H 2022. Repetitive marsquakes in Martian upper mantle. *Nat Commun* **13:**1695, doi: 10.1038/s41467-022-29329-x
Taylor J, Teanby NA and Wookey J 2013. Estimates of seismic activity in the Cerberus Fossae region of Mars, *J. Geophys. Res. Planets*, **118**:2570– 2581, doi:10.1002/2013JE004469.
Teanby NA, Wookey J 2011. Seismic detection of meteorite impacts on Mars. *Phys. Earth Planet. Inter.* **186:**70–80, doi: 10.1016/j.pepi.2011.03.004
Trebi-Ollennu A., Kim W, Ali K, Khan O, Sorice C. et al. 2018. InSight Mars Lander Robotics Instrument Deployment System. *Space Sci Rev* **214**:93, doi: 10.1007/s11214-018-0520-7
van Driel M, Ceylan S, Clinton JF, Giardini D, Horleston A et al. 2021. High frequency seismic events on Mars observed by InSight, *J. Geophys. Res.: Planets*, **126**:e2020JE006670, doi**:** 10.1029/2020JE006670

van Driel M, Ceylan S, Clinton JF, Giardini D, Alemany H et al. 2019. Preparing for InSight: Evaluation of the Blind Test for Martian Seismicity, *Seismological Research Letters*, **90**:1518-1534, doi: 10.1785/0220180379
Wieczorek MA, Broquet A, McLennan SM, Rivoldini A, Golombek M et al. 2022. InSight constraints on the global character of the Martian crust. *J. Geophys. Res.: Planets*, **127**:e2022JE007298. doi: 10.1029/2022JE007298
Wójcicka N, Collins GS, Bastow ID, Teanby NA, Miljković K et al. 2020. The Seismic Moment and Seismic Efficiency of Small Impacts on Mars. *J. Geophys. Res.: Planets*, **125**: e2020JE006540, doi: 10.1029/2020JE006540
Xu W, Zhu Q and Zhao L 2022. GlitchNet: A Glitch Detection and Removal System for SEIS Records Based on Deep Learning. *Seismological Research Letters*, doi: 10.1785/0220210361
Xiao W and Wang Y 2022. Characteristics of horizontal to vertical spectral ratio of InSight seismic data from Mars. *J. Geophys. Res.: Planets*, **127**:e2020JE006813, doi: 10.1029/2020JE006813
Xu H, Beghein C, Panning MP, Drilleau M, Lognonné P et al. 2020. Measuring Fundamental and Higher Mode Surface Wave Dispersion on Mars From Seismic Waveforms. *Earth and Space Science*, **7**:e2020EA001263. doi: 10.1029/2020EA001263
Xu Z, Stutzmann E, Lognonné P, Schimmel M, Montagner JP and Kawamura T 2022. Radial anisotropy from surface-wave observation in Mars, Europlanet Science Congress 2022, Granada, Spain, 18–23 Sep 2022, EPSC2022-863
Yana C, Hurst K, Kerjean L, Gaudin E, Lognonné P et al. 2022. InSight-SEIS Instrument Deployment Operations on Mars. In: Cruzen, C., Schmidhuber, M., Lee, Y.H. (eds) Space Operations, Springer Aerospace Technology. Springer, Cham, doi: 10.1007/978-3-030-94628-9_29
Zenhäusern G, Stähler SC, Clinton JF, Giardini D, Ceylan S and Garcia RF 2022. Low-Frequency Marsquakes and Where to Find Them: Back Azimuth Determination Using a Polarization Analysis Approach. *Bull. Seis. Soc. America*, doi: 10.1785/0120220019
Zweifel P, Mance D, ten Pierick J, Giardini D, Schmelzbach C et al. 2021. Seismic High-Resolution Acquisition Electronics for the NASA InSight Mission on Mars, *Bull. Seism. Soc. America*, **111**:2909–2923, doi: 10.1785/0120210071